Published for SISSA by Springer

Received: December 14, 2021
Revised: February 28, 2022
Accepted: April 28, 2022
Published: May 24, 2022

JHEP05(2022)155

Cross section measurements of the $e^+e^- \to D^{*+}D^{*-}$ and $e^+e^- \to D^{*+}D^-$ processes at center-of-mass energies from 4.085 to 4.600 GeV

BESIII

The BESIII collaboration

E-mail: besiii-publications@ihep.ac.cn

Abstract: The Born cross sections of the $e^+e^- \to D^{*+}D^{*-}$ and $e^+e^- \to D^{*+}D^-$ processes are measured using e^+e^- collision data collected with the BESIII experiment at center-of-mass energies from 4.085 to 4.600 GeV, corresponding to an integrated luminosity of 15.7 fb^{-1}. The results are consistent with and more precise than the previous measurements by the Belle, Babar and CLEO collaborations. The measurements are essential for understanding the nature of vector charmonium and charmonium-like states.

Keywords: e^+-e^- Experiments, Exotics, Particle and Resonance Production, Quarkonium, Spectroscopy

ArXiv ePrint: 2112.06477

Open Access, © The Authors.
Article funded by SCOAP^3.

https://doi.org/10.1007/JHEP05(2022)155

Contents

1 Introduction

The masses and decay patterns of conventional vector ($J^{PC} = 1^{--}$) charmonium states match well the predictions from the quark potential model [1]. They decay dominantly into open-charm final states when their masses are above the open-charm threshold, such as $\psi(4040)$ and $\psi(4160)$. However, puzzles come when numerous vector charmonium-like states not expected in the quark potential model, such as $Y(4260)$ [2–5] and $Y(4360)$ [6–8], have been observed. Later, more precise data indicates that the line shape of $Y(4260)$ is asymmetric and its mass is close to $4220\,\mathrm{MeV}/c^2$ [9–11]. The measured masses of these charmonium-like states are above the open-charm threshold. In contrast to conventional states at the same energy region, they mainly decay into hidden-charm final states. However, the state around $4220\,\mathrm{MeV}/c^2$ which was observed in open-charm production process $e^+e^- \to Y(4220) \to \pi^+ D^0 \bar{D}^{*-}$ in the BESIII experiment [12] is consistent with previous observations of the $Y(4220)$ state [9–11]. A closer examination of these states in open-charm channels may provide further insights on the nature of these states and offer necessary inputs to different theoretical interpretations including compact tetraquarks, molecules, hybrids, or hadrocharmonia [13–19].

The previously measured cross sections of $e^+e^- \to D^{*+}D^{*-}$ and $e^+e^- \to D^{*+}D^-$ at energy points from 3.875 to 6 GeV [20–23] have been used to understand the vector charmonium(-like) states. Authors of ref. [24] found that the cross sections of the $e^+e^- \to D^{*+}D^{*-}$ process can be described well by the conventional charmonium states $\psi(4040)$, $\psi(4160)$, $\psi(4415)$, and a $\bar{D}D_1(2420)$ hadronic molecule hypothesis of the $Y(4260)$. Authors of ref. [25] used a coupled-channel approach to perform a simultaneous fit to the data in the

JHEP05(2022)155

open-charm channels including $e^+e^- \to D^{*+}D^{*-}$ and $e^+e^- \to D^{*+}D^-$. The fit provides a remarkably good overall description of all the line shapes, with five vector charmonium resonances, $\psi(2S)$, $\psi(3770)$, $\psi(4040)$, $\psi(4160)$, and $\psi(4415)$. Recently, extensive numerical analyses were performed in ref. [26] by combining all the cross sections of the final states $J/\psi\pi^+\pi^-$, $h_c\pi^+\pi^-$, $D^0D^{*-}\pi^+$, $\psi(2S)\pi^+\pi^-$, $\omega\chi_{c0}$, and $J/\psi\eta$ measured in the BESIII, Belle, and BaBar experiments, together with those of the open-charm final states $D^{*+}D^{*-}$ and $D^{*+}D^-$ measured by Belle (with and without $D_s^{*+}D_s^{*-}$ channel). It is concluded that the $Y(4260)$ may be interpreted as a mixture of 4^3S_1 and $3^3D_1(2^3D_1)$ charmonium states. However, more precise measurements are necessary to verify these conclusions.

In this article, we present improved measurements of the Born cross sections of the $e^+e^- \to D^{*+}D^{*-}$ and $e^+e^- \to D^{*+}D^-$ processes at 28 center-of-mass (c.m.) energies ($\sqrt{s}$) from 4.085 to 4.600 GeV.

2 BESIII detector and data samples

The data were collected by the BESIII detector [27], and the total integrated luminosity is 15.7 fb^{-1}. The c.m. energies were measured using $e^+e^- \to \mu^+\mu^-$ events with an uncertainty of 0.8 MeV [28] and the integrated luminosities were measured using Bhabha scattering events to an uncertainty of 1.0% [29, 30]. The data samples used in this analysis and the corresponding integrated luminosities are listed in tables 1 and 2.

The BESIII detector [27] records symmetric e^+e^- collisions provided by the BEPCII storage ring [31], which operates with a peak luminosity of 1×10^{33} cm^{-2}s^{-1} in the c.m. energy range from 2.0 to 4.95 GeV [32]. The cylindrical core of the BESIII detector covers 93% of the full solid angle and consists of a helium-based multilayer drift chamber (MDC), a plastic scintillator time-of-flight system (TOF), and a CsI(Tl) electromagnetic calorimeter (EMC), which are all enclosed in a superconducting solenoidal magnet providing a 1.0 T magnetic field. The solenoid is supported by an octagonal flux-return yoke with resistive plate counter muon identification modules interleaved with steel. The charged-particle momentum resolution at 1 GeV/c is 0.5%, and the dE/dx resolution is 6% for electrons from Bhabha scattering. The EMC measures photon energies with a resolution of 2.5% (5%) at 1 GeV in the barrel (end cap) region. The time resolution in the TOF barrel region is 68 ps, while that in the end cap region is 110 ps. The end cap TOF system was upgraded in 2015 using multi-gap resistive plate chamber technology, providing a time resolution of 60 ps [33–35].

Simulated data samples produced with a GEANT4-based [36] Monte Carlo (MC) package, which includes the geometric description of the BESIII detector and the detector response, are used to determine detection efficiencies and to estimate background contributions. The simulation models, including the beam energy spread, initial state radiation (ISR), and vacuum polarization in the e^+e^- annihilations are treated with the generator KKMC [37, 38]. The ISR of the initial particle affects the detection efficiency and line shape of cross sections, thus, the ISR correction is necessary in the Born cross section measurements and fulfilled by the KKMC generator.

JHEP05(2022)155

$\sqrt{s}$ (GeV)	$\mathcal{L}_{\rm int}$ (pb^{-1})	$\lvert 1-\Pi\rvert^{-2}$	$N^{\rm sig}_{D^{*+}}$	$\epsilon_{D^{*+}}$	$(1+\delta)_{D^{*+}}$	$\sigma^{\rm B}_{D^{*+}}$ (pb)	$N^{\rm sig}_{D^{*-}}$	$\epsilon_{D^{*-}}$	$(1+\delta)_{D^{*-}}$	$\sigma^{\rm B}_{D^{*-}}$ (pb)	$\sigma^{\rm O}_{a}$ (pb)	$\sigma^{\rm B}_{a}$ (pb)
4.0854	52.9	1.051	188±15	0.055±0.001	0.80±0.01	2867±228±147	194±16	0.054±0.001	0.80±0.01	3009±241±149	2471±210	2936±251
4.1285	393.4	1.052	2374±53	0.082±0.001	0.82±0.01	3205±72±167	2379±53	0.083±0.001	0.83±0.01	3121±70±159	2745±152	3159±177
4.1574	406.9	1.053	3086±61	0.100±0.001	0.85±0.01	3177±63±164	2972±60	0.100±0.001	0.85±0.01	3052±61±154	2785±150	3107±170
4.1780	3189.0	1.054	25370±171	0.120±0.001	0.89±0.01	2652±18±122	25697±171	0.120±0.001	0.88±0.02	2701±18±137	2491±116	2662±126
4.1886	570.0	1.056	4358±72	0.121±0.001	0.90±0.01	2496±41±119	4276±71	0.122±0.001	0.91±0.01	2394±40±119	2332±119	2447±126
4.1989	526.0	1.056	3608±65	0.125±0.001	0.95±0.01	2046±37±98	3651±66	0.126±0.001	0.93±0.01	2081±37±104	2050±106	2060±107
4.2092	572.1	1.057	3318±64	0.128±0.001	1.00±0.01	1600±31±84	3440±65	0.128±0.001	0.98±0.02	1689±32±91	1723±92	1638±92
4.2171	569.2	1.056	2653±59	0.127±0.001	1.14±0.01	1136±25±55	2710±59	0.124±0.001	1.16±0.02	1170±26±58	1401±73	1150±62
4.2263	1100.9	1.056	4150±77	0.137±0.001	1.29±0.01	754±14±36	3890±74	0.136±0.001	1.39±0.02	665±13±32	994±50	696±36
4.2357	530.3	1.056	1233±48	0.128±0.001	1.99±0.05	323±12±18	1188±45	0.126±0.001	1.89±0.05	332±13±19	671±42	327±23
4.2438	538.1	1.056	1030±45	0.123±0.001	2.13±0.05	258±11±15	954±44	0.123±0.001	2.19±0.06	234±11±13	559±37	245±18
4.2580	828.4	1.054	1474±52	0.133±0.001	1.92±0.06	247±9±14	1561±57	0.135±0.001	1.92±0.06	258±9±15	510±31	252±17
4.2668	531.1	1.053	990±43	0.135±0.001	1.67±0.01	295±13±16	1032±43	0.134±0.001	1.62±0.01	318±13±15	530±34	307±20
4.2777	175.7	1.053	338±23	0.135±0.001	1.50±0.03	336±23±19	367±25	0.136±0.001	1.45±0.01	375±25±19	551±43	355±29
4.2879	491.5	1.053	1074±40	0.138±0.001	1.25±0.01	452±17±23	1079±40	0.137±0.001	1.25±0.01	455±17±23	596±37	454±28
4.3079	45.1	1.052	118±13	0.157±0.001	1.16±0.04	511±55±32	158±14	0.164±0.001	1.04±0.03	726±65±43	693±67	593±65
4.3121	492.1	1.052	1453±43	0.156±0.001	1.02±0.01	661±20±33	1496±44	0.155±0.001	1.08±0.01	645±19±31	720±40	652±36
4.3374	501.1	1.051	1998±49	0.169±0.001	0.98±0.01	854±21±43	1980±49	0.168±0.001	0.96±0.01	869±21±43	882±48	861±48
4.3583	543.9	1.051	2550±55	0.183±0.001	0.95±0.02	958±21±49	2555±55	0.186±0.001	0.96±0.01	937±20±44	950±50	945±50
4.3774	522.8	1.051	2403±53	0.181±0.001	0.96±0.02	946±21±49	2507±54	0.179±0.001	0.95±0.01	1001±21±51	972±51	973±54
4.3874	55.6	1.051	323±19	0.195±0.001	0.90±0.02	1180±70±63	259±18	0.190±0.001	1.01±0.01	868±59±41	1003±71	960±74
4.3964	505.0	1.051	2462±53	0.185±0.001	0.98±0.01	959±21±46	2403±53	0.188±0.001	0.95±0.02	951±21±50	968±51	956±52
4.4156	1090.7	1.052	4963±76	0.193±0.001	0.99±0.01	845±13±40	4963±76	0.193±0.001	1.01±0.01	833±13±40	883±44	839±42
4.4362	568.1	1.054	2211±52	0.189±0.001	1.06±0.01	690±16±34	2397±54	0.192±0.001	1.03±0.01	759±17±36	797±41	721±38
4.4671	111.1	1.055	327±20	0.188±0.001	1.20±0.02	465±29±23	333±21	0.188±0.001	1.22±0.01	463±29±22	591±43	464±34
4.5271	112.1	1.054	280±19	0.191±0.001	1.18±0.03	394±27±20	302±20	0.198±0.001	1.13±0.02	428±28±22	500±37	409±33
4.5745	48.9	1.054	145±13	0.206±0.001	1.07±0.01	475±44±23	145±13	0.201±0.001	1.13±0.01	462±42±23	543±49	468±43
4.5995	586.9	1.055	1479±43	0.204±0.001	1.17±0.01	373±11±18	1473±43	0.202±0.001	1.16±0.01	381±11±18	463±25	377±20

Table 1. The Born cross section of $e^+e^- \to D^{*+}D^{*-}$, $\sigma^{\rm B}$, together with the integrated luminosity $\mathcal{L}_{\rm int}$, the vacuum polarization factor $\lvert 1-\Pi\rvert^{-2}$, the number of signal events $N^{\rm sig}$, the reconstruction efficiency ϵ, and the ISR correction factor $(1+\delta)$. The subscripts D^{*+}, D^{*-}, and a denote the results for the reconstructed D^{*+} candidates, reconstructed D^{*-} candidates, and the average values, respectively. The observed cross sections of the average values without ISR and vacuum polarization corrections are represented by $\sigma^{\rm O}_a$. The first uncertainties in $\sigma^{\rm B}_{D^{*+}}$ and $\sigma^{\rm B}_{D^{*-}}$ are statistical and the second systematic; the uncertainties in $\sigma^{\rm B}_a$ and $\sigma^{\rm O}_a$ include the statistical and systematic uncertainties calculated using the same method as in ref. [39]. The uncertainties in $N^{\rm sig}$ and ϵ are statistical; the uncertainties in $(1+\delta)$ are the systematic uncertainties involved with ISR correction factor (see below).

JHEP05(2022)155

$\sqrt{s}$ (GeV)	$\mathcal{L}_{\rm int}$ (pb^{-1})	$\lvert 1-\Pi\rvert^{-2}$	$N^{\rm sig}_{D^{*+}}$	$\epsilon_{D^{*+}}$	$(1+\delta)_{D^{*+}}$	$\sigma^{\rm B}_{D^{*+}}$ (pb)	$N^{\rm sig}_{D^{*-}}$	$\epsilon_{D^{*-}}$	$(1+\delta)_{D^{*-}}$	$\sigma^{\rm B}_{D^{*-}}$ (pb)	$\sigma^{\rm O}_{c}$ (pb)	$\sigma^{\rm B}_{c}$ (pb)
4.0854	52.9	1.051	176±14	0.135±0.001	0.93±0.01	947±76±50	161±13	0.131±0.001	0.98±0.02	850±70±44	1790±77	1783±79
4.1285	393.4	1.052	1031±34	0.141±0.001	1.05±0.01	627±21±31	1070±35	0.141±0.001	1.00±0.01	681±22±33	1413±41	1303±38
4.1574	406.9	1.053	1074±35	0.160±0.001	1.01±0.02	581±19±31	1137±36	0.156±0.001	1.00±0.01	632±20±31	1284±37	1217±36
4.1780	3189.0	1.054	8634±101	0.173±0.001	1.04±0.01	536±6±26	8467±100	0.173±0.001	1.05±0.01	518±6±26	1159±29	1052±26
4.1886	570.0	1.056	1375±40	0.171±0.001	1.09±0.01	460±14±22	1425±41	0.171±0.001	1.06±0.01	489±14±23	1075±30	948±26
4.1989	526.0	1.056	1298±39	0.178±0.001	1.06±0.01	462±14±23	1275±39	0.175±0.001	1.06±0.01	460±14±22	1037±29	923±26
4.2092	572.1	1.057	1284±39	0.178±0.001	1.12±0.01	400±12±20	1277±39	0.175±0.001	1.11±0.01	409±12±20	948±27	808±23
4.2171	569.2	1.056	1258±39	0.180±0.001	1.12±0.01	389±12±19	1270±38	0.179±0.001	1.12±0.01	393±12±19	925±26	781±22
4.2263	1100.9	1.056	2460±54	0.194±0.001	1.15±0.01	356±8±17	2342±53	0.192±0.001	1.18±0.01	331±8±16	843±22	684±18
4.2357	530.3	1.056	1211±38	0.194±0.001	1.08±0.01	385±12±18	1139±37	0.192±0.001	1.12±0.01	356±11±17	859±24	739±21
4.2438	538.1	1.056	1159±37	0.196±0.001	1.11±0.01	351±11±17	1188±37	0.195±0.001	1.09±0.01	367±12±18	834±24	715±20
4.2580	828.4	1.054	2003±49	0.208±0.001	1.07±0.01	385±9±19	1875±47	0.207±0.001	1.09±0.01	356±9±18	841±23	738±20
4.2668	531.1	1.053	1301±39	0.208±0.001	1.05±0.01	397±12±19	1280±39	0.207±0.001	1.04±0.01	396±12±19	876±24	793±22
4.2777	175.7	1.053	420±22	0.205±0.001	1.06±0.01	390±21±19	471±23	0.209±0.001	0.98±0.02	464±23±24	913±30	834±29
4.2879	491.5	1.053	1165±37	0.204±0.001	1.06±0.01	391±13±19	1167±37	0.203±0.001	1.07±0.01	387±12±18	871±24	778±22
4.3079	45.1	1.052	109±11	0.224±0.001	1.08±0.01	355±37±18	103±11	0.224±0.001	1.08±0.03	333±35±19	780±39	688±36
4.3121	492.1	1.052	1081±36	0.211±0.001	1.13±0.01	327±11±16	1145±37	0.212±0.001	1.03±0.01	376±12±18	797±23	691±20
4.3374	501.1	1.051	1174±37	0.223±0.001	1.04±0.01	360±11±17	1150±37	0.224±0.001	1.08±0.02	339±11±17	775±22	699±20
4.3583	543.9	1.051	1341±40	0.242±0.001	1.06±0.01	343±10±16	1322±39	0.236±0.001	1.07±0.01	342±10±17	766±21	685±19
4.3774	522.8	1.051	1257±38	0.233±0.001	1.05±0.01	351±11±17	1218±38	0.231±0.001	1.05±0.01	342±11±16	762±21	692±19
4.3874	55.6	1.051	137±13	0.246±0.001	1.08±0.01	332±30±16	146±13	0.248±0.001	1.02±0.01	371±34±18	770±35	697±32
4.3964	505.0	1.051	1189±38	0.238±0.001	1.05±0.01	334±11±16	1276±38	0.240±0.001	1.01±0.02	370±11±19	759±21	692±20
4.4156	1090.7	1.052	2689±56	0.245±0.001	1.04±0.01	344±7±16	2671±55	0.246±0.001	1.06±0.01	334±7±16	748±19	677±17
4.4362	568.1	1.054	1447±41	0.250±0.001	1.02±0.01	355±10±17	1388±40	0.248±0.001	1.04±0.01	337±10±16	749±21	690±19
4.4671	111.1	1.055	281±18	0.253±0.001	1.03±0.01	345±22±16	266±17	0.253±0.001	1.06±0.01	318±21±15	727±26	660±24
4.5271	112.1	1.054	260±17	0.261±0.001	1.08±0.01	290±19±14	256±17	0.265±0.001	1.06±0.01	288±19±14	654±24	579±22
4.5745	48.9	1.054	77±10	0.255±0.001	1.24±0.03	177±22±10	104±11	0.266±0.001	1.11±0.01	255±26±13	518±28	414±23
4.5995	586.9	1.055	1090±36	0.268±0.001	1.10±0.01	224±7±11	1144±37	0.269±0.001	1.12±0.02	229±7±12	529±15	451±13

Table 2. The Born cross sections of $e^+e^- \to D^{*+}D^-$ ($\sigma^{\rm B}_{D^{*+}}$) and $e^+e^- \to D^{*-}D^+$ ($\sigma^{\rm B}_{D^{*-}}$), together with the integrated luminosity $\mathcal{L}_{\rm int}$, the vacuum polarization factor $|1-\Pi|^{-2}$, the number of signal events $N^{\rm sig}$, the reconstruction efficiency ϵ, and the ISR correction factor $(1+\delta)$. The subscripts D^{*+}, D^{*-}, and c denote the results for the reconstructed D^{*+} candidates, reconstructed D^{*-} candidates, and the combined values, respectively. The observed cross sections of the combined values without ISR and vacuum polarization corrections are represented by $\sigma^{\rm O}_c$. The first uncertainties in $\sigma^{\rm B}_{D^{*+}}$ and $\sigma^{\rm B}_{D^{*-}}$ are statistical and the second systematic; the uncertainties in $\sigma^{\rm B}_c$ and $\sigma^{\rm O}_c$ include the statistical and systematic uncertainties calculated using the same method as in ref. [39]. The uncertainties in $N^{\rm sig}$ and ϵ are statistical; the uncertainties in $(1+\delta)$ are the systematic uncertainties involved with ISR correction factor (see below).

JHEP05(2022)155

Exclusively generated MC samples			
$e^+e^- \to D^{*+}\bar{D}^0\pi^-$,	$D^{*+} \to \pi^+D^0$,	$D^0 \to K^-\pi^+$,	$\bar{D}^0 \to$ anything
$e^+e^- \to D^{*-}D^0\pi^+$,	$D^0 \to K^-\pi^+$	$D^{*-} \to$ anything	
$e^+e^- \to D^{*+}\bar{D}^{*0}\pi^-$,	$D^{*+} \to \pi^+D^0$	$D^0 \to K^-\pi^+$,	$\bar{D}^{*0} \to$ anything
$e^+e^- \to D^{*-}D^{*0}\pi^+$,	$D^{*0} \to \pi^0D^0(\gamma D^0)$,	$D^0 \to K^-\pi^+$,	$D^{*-} \to$ anything
$e^+e^- \to D^{*+}D^-\pi^0$,	$D^{*+} \to \pi^+D^0$	$D^0 \to K^-\pi^+$,	$D^- \to$ anything
$e^+e^- \to D^-D^0\pi^+$,	$D^0 \to K^-\pi^+$,	$D^- \to$ anything	
$e^+e^- \to D^{*0}\bar{D}^{*0}$,	$D^{*0} \to$ anything,	$\bar{D}^{*0} \to$anything	

Table 3. The decay chains of the exclusively generated MC samples for background studies.

The signal MC samples of the $e^+e^- \to D^{*+}D^{*-}$ and $e^+e^- \to D^{*+}D^-$ processes with 100,000 events are generated using phase-space (PHSP) [40, 41] and helicity-amplitude (HELAMP) [40, 41] models at each c.m. energy, respectively. These signal models describe data well at each energy point. The D^{*+} meson is reconstructed by using the decay chain $D^{*+} \to \pi^+D^0$, $D^0 \to K^-\pi^+$, while the D^{*-} or D^- is not reconstructed exclusively but is inferred from energy-momentum conservation. Inclusion of charge-conjugated (*c.c.*) states is implicit unless otherwise stated.

Generic MC samples spread over the complete energy range are used to analyze the possible background contributions. The generic MC sample includes the production of open-charm processes, the ISR production of vector charmonium(-like) states, and the continuum processes incorporated in KKMC [37, 38]. The known decay modes are modelled with EVTGEN [40, 41] using branching fractions taken from the Particle Data Group [42], and the remaining unknown charmonium decays are modelled with LUNDCHARM [43, 44]. Final-state radiation (FSR) from charged final-state particles is incorporated using PHOTOS [45].

In addition, exclusive MC samples with 100,000 events each for the processes $e^+e^- \to D^{*+}\bar{D}^0\pi^-$, $D^{*-}D^0\pi^+$, $D^{*+}\bar{D}^{*0}\pi^-$, $D^{*-}D^{*0}\pi^+$, $D^{*+}D^-\pi^0$, $D^0D^-\pi^+$, and $D^{*0}\bar{D}^{*0}$ (listed in table 3) are generated with PHSP model at each c.m. energy to study possible background contributions. Here $e^+e^- \to D^{*+}\bar{D}^0\pi^-$ and $D^{*-}D^0\pi^+$, and $e^+e^- \to D^{*+}\bar{D}^{*0}\pi^-$ and $D^{*0}D^{*-}\pi^+$ are two pairs of charge-conjugated modes, which have the same input line shapes of cross sections. The background contributions at all the energy points are found to be the same.

3 Event selection and background analysis

Candidate events with at least two pions with positive charge and at least one kaon with negative charge are selected. The charged tracks are required to be well reconstructed in the MDC with a polar angle θ satisfying $|\cos\theta| < 0.93$, and the distances of the closest approach to the interaction point in $x-y$ plane and z direction of e^+e^- c.m. frame have to be less than 1 cm and 10 cm, respectively. The particle identification (PID) of kaons and pions is based on the $\mathrm{d}E/\mathrm{d}x$ and time of flight information. Assumption of a given

JHEP05(2022)155

particle identification is based on the larger of the two PID-hypothese probabilities $\mathrm{P}(h)$, $h = K, \pi$. Kaon candidates are required to satisfy $\mathrm{P}(K) > \mathrm{P}(\pi)$ and $\mathrm{P}(K) > 0.001$ with momenta larger than 0.3 GeV/c. Pion candidates are required to satisfy $\mathrm{P}(\pi) > \mathrm{P}(K)$ and $\mathrm{P}(\pi) > 0.001$. The pions with momenta less than 0.3 GeV/c are named as π_L^+, whereas the ones with momenta larger than 0.3 GeV/c are named as π_H^+. At least one π_L^+ and one π_H^+ are required in the final states.

We assume each input charged track originated from a common vertex, and a kinematic fit is performed to the $K^-\pi_H^+$ candidates, which constrains the masses of the $K^-\pi_H^+$ candidates to the known mass of the D^0 meson [42], to improve the track momentum resolution and to reduce background events. If there are multiple candidates in one event, we choose the $K^-\pi_H^+\pi_L^+$ combination with the smallest vertex and kinematic fit χ^2 and require $\chi^2 < 200$ for further studies. To identify signal candidates that involve the D^0 meson, we select events with a $K^-\pi_H^+$ invariant mass before the kinematic fit within a window of three standard deviations ($\pm 3\sigma$) around the D^0 known mass, $1845.4 < M(K^-\pi_H^+) < 1885.2\,\mathrm{MeV}/c^2$, referred to as the D^0 mass window. Here σ is the measured mass resolution of D^0 meson. For the sake of simplicity, we use π^+ to replace π_L^+ in the following text.

After imposing all the requirements mentioned above, we use the two-dimensional (2D) distributions of the π^+D^0 invariant mass $M(\pi^+D^0)$ and recoil mass $RM(\pi^+D^0)$ after the kinematic fit, to study the signal and background contributions. Figure 1 shows the distributions of $RM(\pi^+D^0)$ versus $M(\pi^+D^0)$ for data, signal MC samples of $e^+e^- \to D^{*+}D^{*-}$ and $D^{*+}D^-$, and background MC samples of $e^+e^- \to D^{*+}\bar{D}^0\pi^-$, $D^{*-}D^0\pi^+$, $D^{*+}\bar{D}^{*0}\pi^-$, $D^{*0}D^{*-}\pi^+$, $D^{*+}D^-\pi^0$, $D^0D^-\pi^+$, and $e^+e^- \to D^{*0}\bar{D}^{*0}$ at 4.416 GeV, respectively.

The remaining background contributions are shown in figure 2 together with the fit results where an Argus function [46] and a second-order Chebyshev polynomial are used to fit the $M(\pi^+D^0)$ and $RM(\pi^+D^0)$ distributions, respectively.

4 Signal yield determination

Two-dimensional unbinned fits to the recoil mass $RM(\pi^+D^0)$ versus the invariant mass $M(\pi^+D^0)$ distributions are performed to determine the signal yields of the $e^+e^- \to D^{*+}D^{*-}$ and $D^{*+}D^-$ processes. A 2D probability density function (PDF) $f(M, RM)$ is used to describe the data, where

$$\begin{aligned} f(M,RM) = {} & N^{\mathrm{sig1}} s_1(M,RM) + N^{\mathrm{sig2}} s_2(M,RM) \\ & + N^{\mathrm{bkg1}} \left[\frac{R_1}{1+R_1} b_1(M,RM) + \frac{1}{1+R_1} b_2(M,RM) \right] \\ & + N^{\mathrm{bkg2}} \left[\frac{R_2}{1+R_2} b_3(M,RM) + \frac{1}{1+R_2} b_4(M,RM) \right] \\ & + N^{\mathrm{bkg3}} b_5(M,RM) + N^{\mathrm{bkg4}} b_6(M,RM) \\ & + N^{\mathrm{bkg5}} b_7(M,RM) + N^{\mathrm{bkg6}} b_8(M) b_9(RM). \end{aligned} \tag{4.1}$$

Here, $s_1(M, RM)$ and $s_2(M, RM)$ are the signal PDFs for the $e^+e^- \to D^{*+}D^{*-}$ and $D^{*+}D^-$ processes, respectively, and are modeled using the signal MC shapes convolved with corresponding Gaussian functions. The parameters of the Gaussian functions reflect the

JHEP05(2022)155

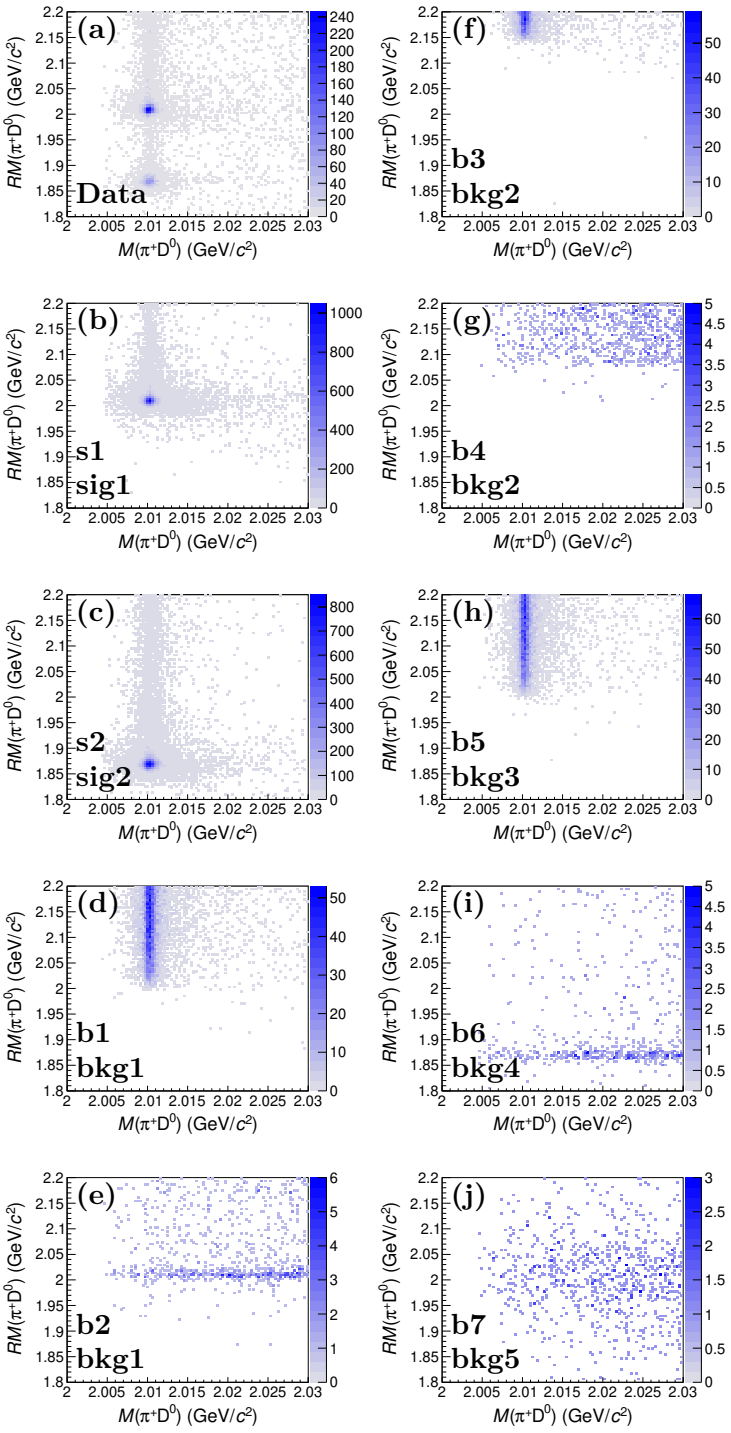

Figure 1. Distributions of the recoil mass $RM(\pi^+D^0)$ versus the invariant mass $M(\pi^+D^0)$ for (a) data, and the MC-simulated processes (b) $e^+e^- \to D^{*+}D^{*-}$, (c) $D^{*+}D^-$, (d) $D^{*+}\bar{D}^0\pi^-$, (e) $D^{*-}D^0\pi^+$, (f) $D^{*+}\bar{D}^{*0}\pi^-$, (g) $D^{*-}D^{*0}\pi^+$, (h) $D^{*+}D^-\pi^0$, (i) $D^-D^0\pi^+$, and (j) $D^{*0}\bar{D}^{*0}$ at 4.416 GeV c.m. energy, where plots (b) and (c) are the signal processes, and plots (d-j) are the background processes in this analysis. Labels of s1, sig1, b1, bkg1 etc. are used in eq. (4.1) and described in text.

JHEP05(2022)155

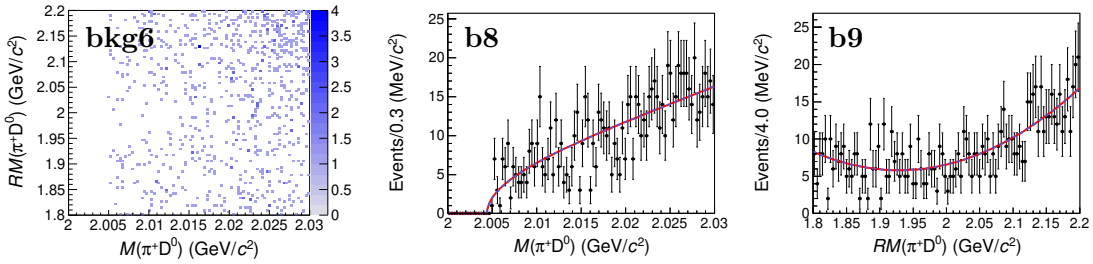

Figure 2. Distribution of the recoil mass $RM(\pi^+D^0)$ versus the invariant mass $M(\pi^+D^0)$ and the 2D fit result for the remaining background contributions of the generic MC samples after removing signal events and peaking background contributions mentioned in the text at 4.416 GeV c.m. energy. An Argus function and a second-order Chebyshev polynomial (red lines) are used to fit the $M(\pi^+D^0)$ and $RM(\pi^+D^0)$ distributions, respectively. Labels of bkg6, b8, and b9 are used in eq. (4.1) and described in text.

differences in the mass resolution between MC simulation and data, and are obtained from one-dimensional (1D) fits to the $M(\pi^+D^0)$ and $RM(\pi^+D^0)$ distributions. The $b_1(M, RM)$, $b_2(M, RM)$, $b_3(M, RM)$, $b_4(M, RM)$, $b_5(M, RM)$, $b_6(M, RM)$, and $b_7(M, RM)$ are the PDFs of the background processes $e^+e^- \to D^{*+}\bar{D}^0\pi^-$, $D^{*-}D^0\pi^+$, $D^{*+}\bar{D}^{*0}\pi^-$, $D^{*-}D^{*0}\pi^+$, $D^{*+}D^-\pi^0$, $D^-D^0\pi^+$, and $D^{*0}\bar{D}^{*0}$ and are shown in figure 1(d-j). The $b_8(M)$ and $b_9(RM)$ are the Argus function and second-order Chebyshev polynomial mentioned before. The PDFs of signal and background processes in eq. (4.1) which are affected by the ISR effect are changed with different c.m. energies, especially the signal PDFs of $e^+e^- \to D^{*+}D^{*-}$. Its radiative tail in the $RM(\pi^+D^0)$ distribution is appearing or vanishing with the sharply changed cross sectional line shape of $e^+e^- \to D^{*+}D^{*-}$. We use these different PDFs to perform the 2D fit at different energy points.

The numbers of the signal events of $e^+e^- \to D^{*+}D^{*-}$ and $D^{*+}D^-$, the background events of $e^+e^- \to D^{*+}D^-\pi^0$, $D^-D^0\pi^+$, and $D^{*0}\bar{D}^{*0}$, and the flat background events are represented by $N^{\rm sig1}$, $N^{\rm sig2}$, $N^{\rm bkg3}$, $N^{\rm bkg4}$, $N^{\rm bkg5}$ and $N^{\rm bkg6}$, respectively; $N^{\rm bkg1}$ is the total number of $e^+e^- \to D^{*+}\bar{D}^0\pi^-$ and $D^{*-}D^0\pi^+$ events, and $N^{\rm bkg2}$ the total number of $e^+e^- \to D^{*+}\bar{D}^{*0}\pi^-$ and $D^{*-}D^{*0}\pi^+$ events. The ratios between the charge-conjugated modes of $e^+e^- \to D^{*+}\bar{D}^0\pi^-$ and $D^{*-}D^0\pi^+$, and $e^+e^- \to D^{*+}\bar{D}^{*0}\pi^-$ and $D^{*0}D^{*-}\pi^+$ are denoted by R_1 and R_2, according to $R_1 = \mathcal{B}_{\rm bkg1}\epsilon_{\rm bkg1}/\mathcal{B}^{c.c.}_{\rm bkg1}\epsilon^{c.c.}_{\rm bkg1}$ and $R_2 = \mathcal{B}_{\rm bkg2}\epsilon_{\rm bkg2}/\mathcal{B}^{c.c.}_{\rm bkg2}\epsilon^{c.c.}_{\rm bkg2}$, where $\mathcal{B}_{\rm bkg1}$, $\mathcal{B}^{c.c.}_{\rm bkg1}$, $\mathcal{B}_{\rm bkg2}$, and $\mathcal{B}^{c.c.}_{\rm bkg2}$ are the products of branching fractions from the intermediate states for the processes $e^+e^- \to D^{*+}\bar{D}^0\pi^-$, $D^{*-}D^0\pi^+$, $D^{*+}\bar{D}^{*0}\pi^-$, and $D^{*0}D^{*-}\pi^+$, respectively. The corresponding reconstruction efficiencies are $\epsilon_{\rm bkg1}$, $\epsilon^{c.c.}_{\rm bkg1}$, $\epsilon_{\rm bkg2}$, and $\epsilon^{c.c.}_{\rm bkg2}$. All the numbers of events in the 2D fit are left free. The cross feeds from the charge-conjugated modes of signal channels are below 0.02% and therefore are neglected.

The 1D projections of the fit results to the $RM(\pi^+D^0)$ versus $M(\pi^+D^0)$ distributions at 4.416 GeV and the corresponding log-scale plots are shown in figure 3. The distributions at other energy points are fitted using the same method to determine the signal yields, which are summarized in tables 1 and 2.

JHEP05(2022)155

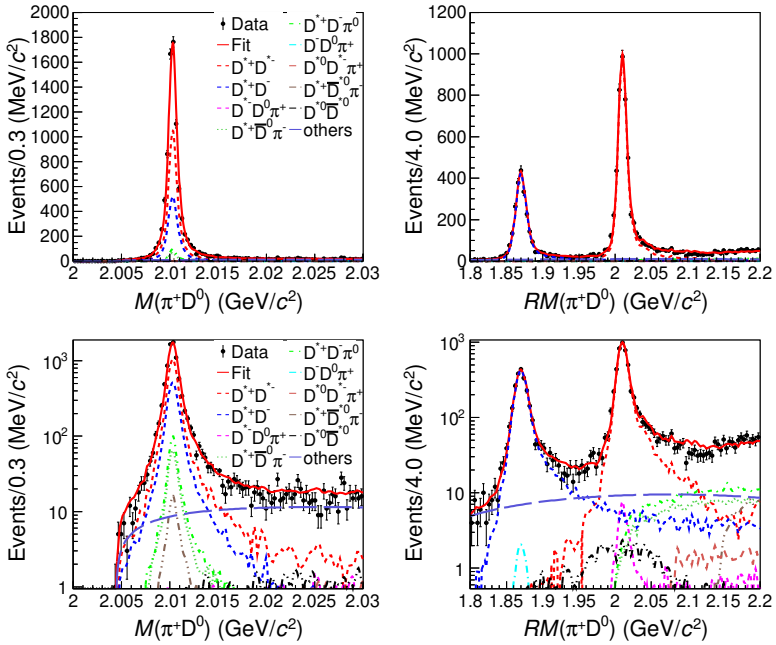

Figure 3. The 1D projections of the 2D fit (top) to the $RM(\pi^+D^0)$ versus $M(\pi^+D^0)$ distributions for the reconstructed D^{*+} candidates at 4.416 GeV and the corresponding log-scale plots (bottom). Dots with error bars are data. The red solid lines represent the fit result; the red and blue dashed lines denote the signal processes of $e^+e^- \to D^{*+}D^{*-}$ and $e^+e^- \to D^{*+}D^-$, respectively; the other dashed lines in different colors represent different background events.

5 Cross section measurements

The Born cross sections of the reaction channels $e^+e^- \to D^{*+}D^{*-}$ and $e^+e^- \to D^{*+}D^-$ are calculated with

$$\sigma^{\rm B} = \frac{N^{\rm sig}}{\mathcal{L}_{\rm int}(1+\delta)|1-\Pi|^{-2}\mathcal{B}_1\mathcal{B}_2\epsilon}, \tag{5.1}$$

where $N^{\rm sig}$ is the signal yield in the 2D fit; $\mathcal{L}_{\rm int}$ is the integrated luminosity; $|1-\Pi|^{-2}$ is the vacuum polarization factor [47]; $\mathcal{B}_1$ and $\mathcal{B}_2$ are the branching fractions of $D^{*+} \to \pi^+D^0$ and $D^0 \to K^-\pi^+$ [42], respectively; $\epsilon = \frac{N^{\rm 2Dfit}}{N^{\rm gen}}$ is the reconstruction efficiency for the $e^+e^- \to D^{*+}D^{*-}$ or $e^+e^- \to D^{*+}D^-$ mode ($N^{\rm 2Dfit}$ and $N^{\rm gen}$ are the numbers of signal events in the 2D fit region and generated events, respectively). The ISR correction factor $(1+\delta)$ follows

$$(1+\delta)|1-\Pi|^{-2} = \frac{\int \sigma^{\rm dressed}(s(1-x))F(x,s)ds}{\sigma^{\rm B}(s)}, \tag{5.2}$$

where $F(x,s)$ is the radiation function obtained from quantum electrodynamics calculation [37, 38, 48], the variable x is the fraction of energy carried by the ISR photon, and $\sigma^{\rm dressed}$ is the cross section without vacuum polarization correction. The cross sectional line shapes of Belle results [21] are used as a starting point to generate the signal MC samples of $e^+e^- \to D^{*+}D^{*-}$ and $D^{*+}D^-$, and obtain the initial reconstruction efficiencies and ISR correction factors for each c.m. energy. The first measured cross sections of

JHEP05(2022)155

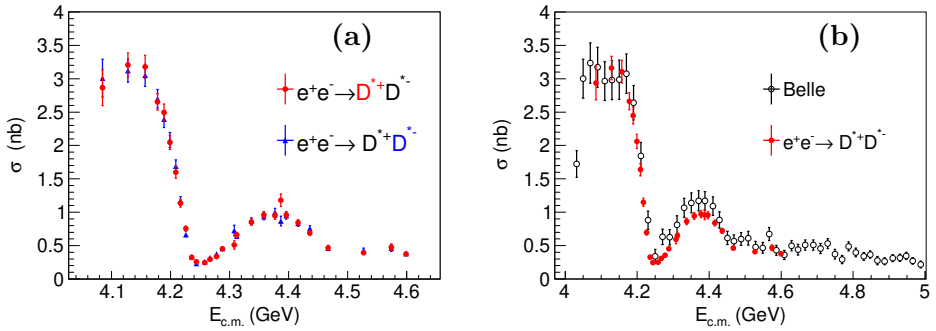

Figure 4. (a) The Born cross sections of $e^+e^- \to D^{*+}D^{*-}$ as a function of the c.m. energy for the reconstructed D^{*+} (red dots) and D^{*-} candidates (blue triangles). (b) The comparison of the average cross sections for $e^+e^- \to D^{*+}D^{*-}$ between this work (red dots) and those of the Belle experiment [21] (black circles). Error bars are the quadratic sum of statistical and systematic uncertainties.

$e^+e^- \to D^{*+}D^{*-}$ and $D^{*+}D^-$ are obtained by above mentioned procedures. Then the line shapes of the first measured cross sections are taken as inputs to re-generate the signal MC samples and re-calculate their efficiencies and ISR correction factors. The 2D fit is re-performed with the updated PDFs of signals. The cross sections of $e^+e^- \to D^{*+}D^{*-}$ and $D^{*+}D^-$ are updated and taken as inputs again for next round. These procedures are repeated until the differences of $(1+\delta)\epsilon$ between two adjacent iterations are less than 3%, then the cross sections are considered to be convergent. The PDFs of MC-simulated signal shapes, efficiencies, ISR correction factors, and the cross sections of the last round are taken as the final results and shown in this paper. The differences of $(1+\delta)\epsilon$ between the last two iterations are taken as the systematic uncertainties of the cross sections convergence. The Born cross sections of $e^+e^- \to D^{*+}D^{*-}$ and $e^+e^- \to D^{*+}D^-$, and the numbers used in the calculation are listed in tables 1 and 2.

The cross sections of $e^+e^- \to D^{*+}D^{*-}$ for different c.m. energy points are shown in figure 4(a) for the reconstructed D^{*+} and D^{*-} events, respectively. They are in agreement with each other within uncertainties. The average cross sections are calculated using the same method as in ref. [39], where correlations between two measurements are considered. Figure 4(b) shows the comparison of the average cross sections of $e^+e^- \to D^{*+}D^{*-}$ between this work and those of the Belle [21] experiment. The results are overall compatible.

The cross sections of $e^+e^- \to D^{*+}D^-$ and $e^+e^- \to D^+D^{*-}$ for different c.m. energy points are shown in figure 5(a). Again, the two results are in good agreement. The cross sections of $e^+e^- \to D^{*+}D^-$ and $e^+e^- \to D^+D^{*-}$ are averaged using the same method as described above. The total cross sections of $e^+e^- \to D^{*+}D^- + c.c.$ are twice the average values. The comparison of the cross section of $e^+e^- \to D^{*+}D^- + c.c.$ between this work and those of the Belle [21] experiment is shown in figure 5(b). They are overall compatible.

JHEP05(2022)155

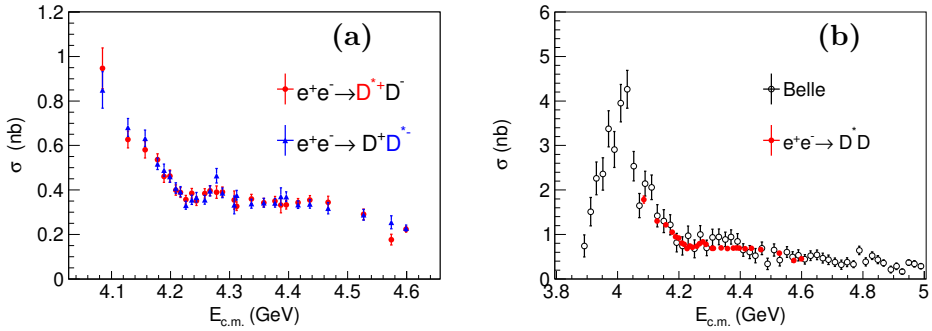

Figure 5. (a) The Born cross sections of the reaction channel $e^+e^- \to D^{*+}D^-$ for the reconstructed D^{*+} candidates (red dots) and $e^+e^- \to D^+D^{*-}$ for the reconstructed D^{*-} candidates (blue triangles) as functions of the c.m. energy. (b) The comparison of the combined cross sections for $e^+e^- \to D^{*+}D^- + c.c.$ between this work (red dots) and those of the Belle experiment [21] (black circles). Error bars are the quadratic sum of statistical and systematic uncertainties.

6 Systematic uncertainties

The systematic uncertainties in the cross-section measurements mainly come from luminosity determination, track reconstruction efficiency, PID efficiency, and the branching fractions of the charmed meson decays, kinematic fit, ISR correction factor, fit range and modeling of the signal and background shapes. The uncertainty from the vacuum polarization is negligible. The uncertainties due to luminosity, track reconstruction efficiency, PID efficiency, and the branching fractions of charmed meson decays are common while the other uncertainties are individual and uncommon for reconstructed D^{*+} and D^{*-} candidates.

- *Luminosity, track reconstruction efficiency, and PID efficiency.* The integrated luminosity is measured using Bhabha scattering events with an uncertainty of 1.0% [29, 30]. The uncertainty of the track reconstruction efficiency is 1.0% per track, taken from ref. [12]. The uncertainty associated with PID efficiency is taken conservatively to be 1.0% per track [12].

- *Branching fractions.* The uncertainties of the branching fractions $\mathcal{B}(D^{*+} \to \pi^+ D^0)$ and $\mathcal{B}(D^0 \to K^-\pi^+)$ are 0.74% and 0.78% [42], respectively.

Therefore, the common systematic uncertainty is 4.49% in this analysis by summing the individual ones in quadrature.

- *Kinematic fit.* The systematic uncertainty from the kinematic fit is estimated by correcting the helix parameters of charged tracks according to the method described in ref. [49]. The signal MC sample with the track helix parameter correction applied is taken as the nominal one. The difference between detection efficiencies obtained from MC samples with and without correction is taken as the systematic uncertainty. It is in the range between 0.86% and 2.40% for different energy points.

JHEP05(2022)155

- *ISR correction factor.* The line shape of the cross section affects the ISR correction factor and the reconstruction efficiency. There are three uncertainties involved in the ISR correction factor. Firstly, the differences of $(1+\delta)\epsilon$ between the last two iterations are taken as the systematic uncertainties of the cross sections convergence (ISR1) and are in the range between 0.00% and 2.71%. Secondly, to consider the statistic of the input lineshape, the input cross section at each energy point is changed randomly by varying the central value within its statistical uncertainty and the value of $(1+\delta)\epsilon$ is recalculated. This process is performed for 1000 times, and a Gaussian function is used to fit the $(1+\delta)\epsilon$ distribution. The width of the Gaussian function represents the systematic uncertainty of the statistic of input cross sectional line shape and varies between 0.01% and 0.60% (ISR2). Lastly, an alternative smooth method of LOWESS [50] is used instead of TSpline3 [51] for the input cross section line shape, and the differences in $(1+\delta)\epsilon$ values, varying between 0.01% to 3.73% (ISR3), are taken as the systematic uncertainties.

- *Fit range.* The systematic uncertainty caused by the choice of the fit range is estimated by varying the upper and lower bounds of the fit range by $\pm$ 10 MeV/c^2. Toy MC samples are generated using the obtained PDFs and the corresponding 2D fits are performed in the new fit range. This process has been repeated for 2000 times. The differences between the input values and the means of the output values are taken as the systematic uncertainties which vary between 0.05% and 1.61%.

- *Background shape.* The uncertainty attributed to the background shape is estimated by changing the background shape in the 2D fit. To reduce influence of statistical fluctuation, we perform the 2D fit to the combined data samples from the reconstructed D^{*+} and D^{*-} candidates, where the PDFs of signal and dominant background processes for the two reconstructed methods are weighted based on the corresponding values of $\sigma^{\rm B}(1+\delta)\epsilon$ from the reconstructed D^{*+} and D^{*-} candidates. The differences of signal yields from 2D fits to the combined data samples by changing the background shape in π^+D^0 recoil mass spectrum from the second-order Chebyshev polynomial to a linear function, are taken as the systematic uncertainties of background shape. The uncertainties due to the Argus function and PDFs of the peaking background contributions are checked and are found to be negligible. The systematic uncertainties due to the background shape are less than 1%.

- *Signal shape.* The parameters of the Gaussian function, i.e., mean and resolution, describe the differences between data and signal MC simulation. The differences of signal yields from 2D fits to the combined data samples as mentioned above by varying the mean and resolution within one standard deviation are assigned as the systematic uncertainties of mean and resolution. The systematic uncertainties are less than 1% or a little more.

- *Signal models.* As we known, the $e^+e^- \to D^{*+}D^{*-}$ process should be proceeded via three independent amplitudes, namely the P-wave with spin $S = 0$, P-wave with

JHEP05(2022)155

$S = 2$, and F-wave with $S = 2$. Actually, the angular distributions of D^{*+} in the e^+e^- c.m. frame and π^+ (decayed from D^{*+}) in D^{*+} frame from signal MC samples of $e^+e^- \to D^{*+}D^{*-}$ ($D^{*+}D^-$) and data samples are checked and found to be consistent at each energy point. The efficiencies of signal MC samples of $e^+e^- \to D^{*+}D^{*-}$ and $D^{*+}D^-$ are reliable. In addition, in the assumption of the relative phase angle between any two amplitudes is zero, we use a HELAMP model which considers the longitudinally and transversely polarized D^{*+} to generate the signal process $e^+e^- \to D^{*+}D^{*-}$. The parameters of HELAMP model are quoted from ref. [21]. The difference of the efficiencies compared to the nominal ones are less than 1%, which are within the MC statistics uncertainties. Thus, the systematic uncertainties of detection efficiencies due to different signal generator models are neglected. The MC-simulated signal PDFs of $e^+e^- \to D^{*+}D^{*-}$ and $D^{*+}D^-$ at different angular regions of D^{*+} in the e^+e^- c.m. frame are stable and the systematic uncertainties of the PDFs of signals at different angular regions can be neglected since we already consider the uncertainties due to the mass resolutions.

All the uncommon systematic uncertainties for the reconstructed D^{*+} and D^{*-} candidates are summarized in tables 4 and 5, respectively. The total uncommon systematic uncertainties at each energy point are the sum of individual ones in quadrature.

7 Summary

A measurement of the cross sections of the $e^+e^- \to D^{*+}D^{*-}$ and $e^+e^- \to D^{*+}D^-$ processes is presented using 28 data samples corresponding to a total integrated luminosity of 15.7 fb^{-1} with c.m. energies between 4.085 and 4.600 GeV. The cross sections are consistent with and more precise than those of the Belle, BaBar, and CLEO experiments. The structures in the cross sections measured by the previous experiments are confirmed. In order to finally reveal the nature of the vector charmonium(-like) states in this energy region, measurements on other two-body open-charm modes such as $D\bar{D}$, $D_s^+D_s^-$, $D_s^+D_s^{*-} + c.c.$, $D_s^{*+}D_s^{*-}$ [52] and multi-body modes such as $\pi D\bar{D}$, $\pi D^*\bar{D} + c.c.$, $\pi\pi D\bar{D}$ are necessary. More sophisticated models with further studies on coupled-channel effect are also needed.

Acknowledgments

The BESIII collaboration thanks the staff of BEPCII and the IHEP computing center for their strong support. This work is supported in part by National Key R&D Program of China under Contracts Nos. 2020YFA0406300, 2020YFA0406400; National Natural Science Foundation of China (NSFC) under Contracts Nos. 11625523, 11635010, 11735014, 11822506, 11835012, 11935015, 11935016, 11935018, 11961141012, 12022510, 12025502, 12035009, 12035013, 12061131003; the Chinese Academy of Sciences (CAS) Large-Scale Scientific Facility Program; Joint Large-Scale Scientific Facility Funds of the NSFC and CAS under Contracts Nos. U1732263, U1832207; CAS Key Research Program of Frontier Sciences under Contract No. QYZDJ-SSW-SLH040; 100 Talents Program of CAS; INPAC

JHEP05(2022)155

$\sqrt{s}$ (GeV)	Kinematic fit		ISR1		ISR2		ISR3		Fit range		Background shape		Mean		Resolution		$T_{\rm uncommon}$	
	$D^{*+}D^{*-}$	$D^{*+}D^{-}$	$D^{*+}D^{*-}$	$D^{*+}D^{-}$	$D^{*+}D^{*-}$	$D^{*+}D^{-}$	$D^{*+}D^{*-}$	$D^{*+}D^{-}$	$D^{*+}D^{*-}$	$D^{*+}D^{-}$	$D^{*+}D^{*-}$	$D^{*+}D^{-}$	$D^{*+}D^{*-}$	$D^{*+}D^{-}$	$D^{*+}D^{*-}$	$D^{*+}D^{-}$	$D^{*+}D^{*-}$	$D^{*+}D^{-}$
4.0854	2.10	2.15	0.35	1.31	0.03	0.13	0.41	0.39	0.72	0.37	0.20	0.54	0.47	0.38	0.77	1.09	2.46	2.87
4.1285	2.40	1.69	0.68	0.61	0.03	0.11	0.36	0.78	0.69	0.41	0.11	0.66	0.08	0.28	0.15	0.05	2.62	2.12
4.1574	1.96	2.07	1.10	2.13	0.01	0.07	0.80	0.02	0.88	0.24	0.03	0.28	0.11	0.07	0.14	0.23	2.55	3.00
4.1780	0.86	1.59	0.32	0.25	0.02	0.06	0.19	0.94	0.15	0.08	0.28	0.69	0.02	0.02	0.04	0.08	0.99	1.99
4.1886	1.40	1.61	0.68	0.49	0.03	0.12	0.46	0.13	0.28	0.56	0.09	0.26	0.05	0.10	0.11	0.23	1.65	1.82
4.1989	1.45	1.79	0.46	1.19	0.04	0.11	0.24	0.56	0.35	0.13	0.18	0.40	0.07	0.12	0.11	0.05	1.59	2.27
4.2092	2.40	1.55	1.21	1.09	0.05	0.14	0.41	0.08	0.41	0.34	0.10	0.26	0.08	0.17	0.09	0.09	2.75	1.96
4.2171	1.53	1.49	0.65	0.48	0.06	0.13	0.14	0.11	0.53	0.24	0.03	0.08	0.14	0.09	0.12	0.14	1.76	1.60
4.2263	1.50	1.79	0.39	0.27	0.09	0.12	0.12	0.25	0.48	0.26	0.04	0.06	0.10	0.03	0.11	0.13	1.63	1.85
4.2357	1.79	1.45	0.57	0.06	0.38	0.13	2.48	0.62	1.31	0.32	0.10	0.04	0.16	0.15	0.41	0.14	3.43	1.63
4.2438	1.99	1.43	0.99	0.05	0.52	0.16	2.18	0.22	1.03	0.37	0.49	0.27	1.01	0.08	0.32	0.06	3.52	1.53
4.2580	1.96	1.69	1.01	0.57	0.30	0.10	2.89	0.09	0.88	0.22	0.16	0.25	0.23	0.10	0.10	0.06	3.77	1.83
4.2668	2.03	1.34	0.39	0.34	0.34	0.13	0.51	0.27	1.61	0.40	0.33	0.13	0.30	0.14	0.49	0.15	2.77	1.49
4.2777	1.99	1.74	1.91	0.38	0.46	0.23	0.93	0.06	0.96	0.18	0.05	0.00	0.48	0.16	0.62	0.23	3.20	1.82
4.2879	1.82	1.39	0.49	0.09	0.15	0.14	0.09	0.29	1.45	0.61	0.02	0.02	0.19	0.15	0.36	0.15	2.42	1.57
4.3079	1.86	1.56	0.41	0.05	0.32	0.34	3.73	1.07	0.17	0.62	0.32	0.15	0.23	0.67	0.24	0.71	4.23	2.25
4.3121	1.83	1.48	0.43	0.10	0.17	0.32	0.61	0.32	0.52	0.39	0.40	0.39	0.14	0.11	0.15	0.13	2.10	1.65
4.3374	1.76	1.41	0.21	0.06	0.06	0.13	1.28	0.20	0.66	0.76	0.19	0.12	0.07	0.05	0.08	0.16	2.29	1.64
4.3583	1.68	1.39	1.59	0.77	0.04	0.12	0.62	0.03	0.27	0.51	0.23	0.24	0.03	0.11	0.09	0.14	2.42	1.70
4.3774	1.20	1.35	1.43	0.85	0.04	0.11	1.60	0.32	0.91	0.31	0.37	0.39	0.01	0.10	0.11	0.22	2.65	1.72
4.3874	1.22	1.44	2.04	0.36	0.15	0.54	1.43	0.12	0.31	0.38	0.23	0.25	0.28	0.17	0.29	0.75	2.83	1.82
4.3964	1.48	1.30	0.59	0.66	0.10	0.19	0.41	0.09	0.17	0.40	0.20	0.20	0.03	0.08	0.08	0.13	1.67	1.54
4.4156	1.26	1.30	0.37	0.26	0.05	0.09	0.77	0.03	0.10	0.17	0.07	0.07	0.02	0.05	0.05	0.05	1.53	1.34
4.4362	1.53	1.68	0.77	0.14	0.07	0.10	0.15	0.14	0.70	0.20	0.25	0.27	0.03	0.06	0.07	0.10	1.88	1.73
4.4671	1.71	1.46	0.86	0.16	0.27	0.21	1.01	0.14	0.30	0.08	0.23	0.08	0.17	0.41	0.28	0.15	2.24	1.56
4.5271	1.20	1.20	0.18	0.56	0.19	0.23	2.11	1.09	0.11	0.32	0.36	0.02	0.61	0.52	0.30	0.23	2.56	1.85
4.5745	1.30	1.32	0.63	0.73	0.17	0.60	0.93	2.27	0.11	0.97	0.68	0.63	0.20	0.41	0.59	0.82	1.96	3.16
4.5995	1.26	1.42	0.18	0.68	0.21	0.23	0.27	0.27	0.19	0.21	0.24	0.12	0.05	0.07	0.18	0.16	1.37	1.64

Table 4. The uncommon systematic uncertainties from kinematic fit, ISR correction factor, fit range, background shape, mean and resolution of signal shape for the reconstructed D^{*+} candidates (in units of %). The symbol $T_{\rm uncommon}$ is the total uncommon systematic uncertainty for the reconstructed D^{*+} candidates at each energy point obtained by summing individual ones in quadrature.

JHEP05(2022)155

$\sqrt{s}$ (GeV)	Kinematic fit		ISR1		ISR2		ISR3		Fit range		Background shape		Mean		Resolution		$T_{\rm uncommon}$	
	$D^{*+}D^{*-}$	$D^{+}D^{*-}$	$D^{*+}D^{*-}$	$D^{+}D^{*-}$	$D^{*+}D^{*-}$	$D^{+}D^{*-}$	$D^{*+}D^{*-}$	$D^{+}D^{*-}$	$D^{*+}D^{*-}$	$D^{+}D^{*-}$	$D^{*+}D^{*-}$	$D^{+}D^{*-}$	$D^{*+}D^{*-}$	$D^{+}D^{*-}$	$D^{*+}D^{*-}$	$D^{+}D^{*-}$	$D^{*+}D^{*-}$	$D^{+}D^{*-}$
4.0854	1.10	1.74	0.62	1.53	0.03	0.17	0.17	0.01	0.78	0.15	0.20	0.54	1.08	0.67	1.03	0.22	2.12	2.49
4.1285	2.19	1.73	0.95	0.35	0.03	0.10	0.13	0.30	0.25	0.15	0.11	0.66	0.15	0.21	0.15	0.15	2.42	1.93
4.1574	2.18	1.75	0.65	0.01	0.01	0.07	0.41	0.47	0.17	0.36	0.03	0.28	0.04	0.12	0.15	0.15	2.33	1.88
4.1780	1.19	1.71	1.91	0.88	0.02	0.06	0.37	0.01	0.55	0.15	0.28	0.69	0.01	0.04	0.01	0.09	2.36	2.05
4.1886	1.87	1.49	0.05	0.18	0.03	0.11	0.14	0.10	0.93	0.05	0.09	0.26	0.07	0.05	0.05	0.20	2.10	1.54
4.1989	2.04	1.17	0.31	0.35	0.04	0.11	0.25	0.27	0.72	0.35	0.18	0.40	0.04	0.10	0.13	0.19	2.21	1.38
4.2092	1.86	1.64	2.07	0.60	0.04	0.13	0.75	0.07	0.58	0.94	0.10	0.26	0.10	0.18	0.09	0.09	2.95	2.01
4.2171	1.31	1.93	1.44	0.29	0.06	0.13	0.46	0.22	0.91	0.48	0.03	0.08	0.09	0.14	0.17	0.12	2.20	2.03
4.2263	1.23	1.71	0.74	0.20	0.11	0.13	0.83	0.58	0.13	0.13	0.04	0.06	0.09	0.09	0.10	0.03	1.67	1.83
4.2357	2.16	1.82	2.08	0.12	0.36	0.14	1.64	0.06	1.06	0.22	0.10	0.04	0.49	0.13	0.70	0.07	3.70	1.85
4.2438	1.81	1.75	2.24	1.11	0.51	0.14	1.46	0.30	1.20	0.37	0.49	0.27	0.48	0.07	0.44	0.12	3.58	2.15
4.2580	1.92	1.69	2.71	1.15	0.33	0.11	1.02	0.53	0.84	0.18	0.16	0.25	0.16	0.05	0.24	0.14	3.60	2.14
4.2668	1.76	1.88	0.34	0.64	0.31	0.13	0.09	0.15	0.21	0.19	0.33	0.13	0.21	0.05	0.32	0.09	1.90	2.01
4.2777	1.88	1.70	0.12	1.06	0.35	0.18	0.22	1.19	0.89	0.14	0.05	0.00	0.53	0.16	0.59	0.41	2.27	2.38
4.2879	2.06	1.47	1.02	0.41	0.15	0.15	0.45	0.05	0.26	0.11	0.02	0.02	0.21	0.16	0.25	0.09	2.38	1.55
4.3079	1.88	1.80	0.72	0.00	0.18	0.36	2.92	2.76	0.21	0.52	0.32	0.15	0.61	0.52	1.28	0.42	3.84	3.42
4.3121	1.18	1.65	0.03	0.41	0.22	0.26	0.60	0.29	0.35	0.31	0.40	0.39	0.21	0.23	0.32	0.14	1.49	1.84
4.3374	1.90	1.58	0.12	1.49	0.06	0.15	0.67	0.77	0.28	0.44	0.19	0.12	0.05	0.05	0.08	0.11	2.04	2.36
4.3583	1.45	1.71	0.13	0.90	0.05	0.12	0.02	0.07	0.27	0.61	0.23	0.24	0.07	0.10	0.12	0.15	1.51	2.05
4.3774	1.53	1.26	1.05	0.03	0.04	0.11	1.06	0.40	0.76	0.38	0.37	0.39	0.06	0.07	0.09	0.19	2.30	1.45
4.3874	1.26	1.76	0.38	0.38	0.24	0.54	0.75	0.22	0.08	0.05	0.23	0.25	0.45	0.87	0.21	0.29	1.63	2.12
4.3964	1.78	1.62	1.86	1.63	0.08	0.18	0.51	0.26	0.26	0.49	0.20	0.20	0.05	0.12	0.08	0.03	2.65	2.38
4.4156	1.58	1.36	0.59	0.21	0.05	0.10	0.42	0.22	0.19	0.07	0.07	0.07	0.06	0.07	0.08	0.10	1.75	1.41
4.4362	1.07	1.64	1.02	0.34	0.06	0.11	0.35	0.02	0.18	0.37	0.25	0.27	0.04	0.05	0.09	0.14	1.56	1.75
4.4671	1.57	1.44	0.22	0.01	0.26	0.22	0.50	0.09	0.09	0.22	0.23	0.08	0.27	0.52	0.31	0.27	1.75	1.59
4.5271	1.48	1.52	0.17	1.07	0.16	0.21	2.15	0.03	0.11	0.46	0.36	0.02	0.27	0.42	0.19	0.35	2.67	2.00
4.5745	1.52	1.37	0.03	1.25	0.18	0.36	0.56	0.15	0.61	1.01	0.68	0.63	0.38	0.55	0.85	1.36	2.09	2.67
4.5995	1.34	1.60	0.22	1.64	0.18	0.26	0.12	0.01	0.16	0.08	0.24	0.12	0.05	0.17	0.20	0.08	1.42	2.31

Table 5. The uncommon systematic uncertainties from kinematic fit, ISR correction factor, fit range, background shape, mean and resolution of signal shape for the reconstructed D^{*-} candidates (in units of %). The symbol $T_{\rm uncommon}$ is the total uncommon systematic uncertainty for the reconstructed D^{*-} candidates at each energy point obtained by summing individual ones in quadrature.

JHEP05(2022)155

and Shanghai Key Laboratory for Particle Physics and Cosmology; ERC under Contract No. 758462; European Union Horizon 2020 research and innovation programme under Contract No. Marie Sklodowska-Curie grant agreement No 894790; German Research Foundation DFG under Contracts Nos. 443159800, Collaborative Research Center CRC 1044, FOR 2359, GRK 214; Istituto Nazionale di Fisica Nucleare, Italy; Ministry of Development of Turkey under Contract No. DPT2006K-120470; National Science and Technology fund; Olle Engkvist Foundation under Contract No. 200-0605; STFC (United Kingdom); The Knut and Alice Wallenberg Foundation (Sweden) under Contract No. 2016.0157; The Royal Society, U.K. under Contracts Nos. DH140054, DH160214; The Swedish Research Council; U.S. Department of Energy under Contracts Nos. DE-FG02-05ER41374, DE-SC-0012069.

Open Access. This article is distributed under the terms of the Creative Commons Attribution License (CC-BY 4.0), which permits any use, distribution and reproduction in any medium, provided the original author(s) and source are credited.

References

[1] T. Barnes, S. Godfrey and E.S. Swanson, *Higher charmonia*, *Phys. Rev. D* **72** (2005) 054026 [hep-ph/0505002] [INSPIRE].

[2] BaBar collaboration, *Observation of a broad structure in the $\pi^+\pi^- J/\psi$ mass spectrum around 4.26 GeV/c^2*, *Phys. Rev. Lett.* **95** (2005) 142001 [hep-ex/0506081] [INSPIRE].

[3] BaBar collaboration, *Study of the reaction $e^+e^- \to J/\psi\pi^+\pi^-$ via initial-state radiation at BaBar*, *Phys. Rev. D* **86** (2012) 051102 [arXiv:1204.2158] [INSPIRE].

[4] Belle collaboration, *Measurement of $e^+e^- \to \pi^+\pi^- J/\psi$ cross-section via initial state radiation at Belle*, *Phys. Rev. Lett.* **99** (2007) 182004 [arXiv:0707.2541] [INSPIRE].

[5] Belle collaboration, *Study of $e^+e^- \to \pi^+\pi^- J/\psi$ and observation of a charged charmonium-like state at Belle*, *Phys. Rev. Lett.* **110** (2013) 252002 [*Erratum ibid.* **111** (2013) 019901] [arXiv:1304.0121] [INSPIRE].

[6] BaBar collaboration, *Evidence of a broad structure at an invariant mass of 4.32 GeV/c^2 in the reaction $e^+e^- \to \pi^+\pi^-\psi(2S)$ measured at BaBar*, *Phys. Rev. Lett.* **98** (2007) 212001 [hep-ex/0610057] [INSPIRE].

[7] Belle collaboration, *Observation of two resonant structures in $e^+e^- \to \pi^+\pi^-\psi(2S)$ via initial state radiation at Belle*, *Phys. Rev. Lett.* **99** (2007) 142002 [arXiv:0707.3699] [INSPIRE].

[8] BaBar collaboration, *Study of the reaction $e^+e^- \to \psi(2S)\pi^-\pi^-$ via initial-state radiation at BaBar*, *Phys. Rev. D* **89** (2014) 111103 [arXiv:1211.6271] [INSPIRE].

[9] BESIII collaboration, *Precise measurement of the $e^+e^- \to \pi^+\pi^- J/\psi$ cross section at center-of-mass energies from 3.77 to 4.60 GeV*, *Phys. Rev. Lett.* **118** (2017) 092001 [arXiv:1611.01317] [INSPIRE].

[10] BESIII collaboration, *Evidence of two resonant structures in $e^+e^- \to \pi^+\pi^- h_c$*, *Phys. Rev. Lett.* **118** (2017) 092002 [arXiv:1610.07044] [INSPIRE].

[11] BESIII collaboration, *Cross section measurements of $e^+e^- \to \omega\chi_{c0}$ from $\sqrt{s} = 4.178$ to 4.278 GeV*, *Phys. Rev. D* **99** (2019) 091103 [arXiv:1903.02359] [INSPIRE].

JHEP05(2022)155

[12] BESIII collaboration, *Evidence of a resonant structure in the $e^+e^- \to \pi^+ D^0 D^{*-}$ cross section between* 4.05 *and* 4.60 *GeV*, *Phys. Rev. Lett.* **122** (2019) 102002 [arXiv:1808.02847] [INSPIRE].

[13] H.-X. Chen, W. Chen, X. Liu and S.-L. Zhu, *The hidden-charm pentaquark and tetraquark states*, *Phys. Rept.* **639** (2016) 1 [arXiv:1601.02092] [INSPIRE].

[14] A. Esposito, A. Pilloni and A.D. Polosa, *Multiquark resonances*, *Phys. Rept.* **668** (2017) 1 [arXiv:1611.07920] [INSPIRE].

[15] R.F. Lebed, R.E. Mitchell and E.S. Swanson, *Heavy-quark QCD exotica*, *Prog. Part. Nucl. Phys.* **93** (2017) 143 [arXiv:1610.04528] [INSPIRE].

[16] A. Ali, J.S. Lange and S. Stone, *Exotics: heavy pentaquarks and tetraquarks*, *Prog. Part. Nucl. Phys.* **97** (2017) 123 [arXiv:1706.00610] [INSPIRE].

[17] S.L. Olsen, T. Skwarnicki and D. Zieminska, *Nonstandard heavy mesons and baryons: experimental evidence*, *Rev. Mod. Phys.* **90** (2018) 015003 [arXiv:1708.04012] [INSPIRE].

[18] F.-K. Guo, C. Hanhart, U.-G. Meißner, Q. Wang, Q. Zhao and B.-S. Zou, *Hadronic molecules*, *Rev. Mod. Phys.* **90** (2018) 015004 [arXiv:1705.00141] [INSPIRE].

[19] N. Brambilla et al., *The XYZ states: experimental and theoretical status and perspectives*, *Phys. Rept.* **873** (2020) 1 [arXiv:1907.07583] [INSPIRE].

[20] BELLE collaboration, *Measurement of the near-threshold $e^+e^- \to D^{(*)\pm} D^{(*)\mp}$ cross section using initial-state radiation*, *Phys. Rev. Lett.* **98** (2007) 092001 [hep-ex/0608018] [INSPIRE].

[21] BELLE collaboration, *Angular analysis of the $e^+e^- \to D^{(*)\pm} D^{(*)\mp}$ process near the open charm threshold using initial-state radiation*, *Phys. Rev. D* **97** (2018) 012002 [arXiv:1707.09167] [INSPIRE].

[22] BABAR collaboration, *Exclusive initial-state-radiation production of the $D\bar{D}$, $D^*\bar{D}$, and $D^*\bar{D}^*$ systems*, *Phys. Rev. D* **79** (2009) 092001 [arXiv:0903.1597] [INSPIRE].

[23] CLEO collaboration, *Measurement of charm production cross sections in e^+e^- annihilation at energies between* 3.97 *and* 4.26 *GeV*, *Phys. Rev. D* **80** (2009) 072001 [arXiv:0801.3418] [INSPIRE].

[24] S.-R. Xue, H.-J. Jing, F.-K. Guo and Q. Zhao, *Disentangling the role of the $Y(4260)$ in $e^+e^- \to D^*\bar{D}^*$ and $D_s^*\bar{D}_s^*$ via line shape studies*, *Phys. Lett. B* **779** (2018) 402 [arXiv:1708.06961] [INSPIRE].

[25] T.V. Uglov, Y.S. Kalashnikova, A.V. Nefediev, G.V. Pakhlova and P.N. Pakhlov, *Exclusive open-charm near-threshold cross sections in a coupled-channel approach*, *JETP Lett.* **105** (2017) 1 [arXiv:1611.07582] [INSPIRE].

[26] Q.-F. Cao, H.-R. Qi, G.-Y. Tang, Y.-F. Xue and H.-Q. Zheng, *On leptonic width of $X(4260)$*, *Eur. Phys. J. C* **81** (2021) 83 [arXiv:2002.05641] [INSPIRE].

[27] BESIII collaboration, *Design and construction of the BESIII detector*, *Nucl. Instrum. Meth. A* **614** (2010) 345 [arXiv:0911.4960] [INSPIRE].

[28] BESIII collaboration, *Measurement of the center-of-mass energies at BESIII via the di-muon process*, *Chin. Phys. C* **40** (2016) 063001 [arXiv:1510.08654] [INSPIRE].

[29] BESIII collaboration, *Precision measurement of the integrated luminosity of the data taken by BESIII at center of mass energies between* 3.810 *GeV and* 4.600 *GeV*, *Chin. Phys. C* **39** (2015) 093001 [arXiv:1503.03408] [INSPIRE].

JHEP05(2022)155

[30] BESIII collaboration, *Luminosity measurements for the R scan experiment at BESIII*, *Chin. Phys. C* **41** (2017) 063001 [arXiv:1702.04977] [INSPIRE].

[31] C. Yu et al., *BEPCII performance and beam dynamics studies on luminosity*, in *Proceedings of the 7th Int. Particle Accelerator Conf.*, IPAC2016, Busan, Korea (2016).

[32] BESIII collaboration, *Future physics programme of BESIII*, *Chin. Phys. C* **44** (2020) 040001 [arXiv:1912.05983] [INSPIRE].

[33] X. Li et al., *Study of MRPC technology for BESIII endcap-TOF upgrade*, *Radiat. Detect. Technol. Meth.* **1** (2017) 13.

[34] Y.-X. Guo et al., *The study of time calibration for upgraded end cap TOF of BESIII*, *Radiat. Detect. Technol. Meth.* **1** (2017) 15.

[35] P. Cao et al., *Design and construction of the new BESIII endcap time-of-flight system with MRPC technology*, *Nucl. Instrum. Meth. A* **953** (2020) 163053.

[36] GEANT4 collaboration, *GEANT4 — a simulation toolkit*, *Nucl. Instrum. Meth. A* **506** (2003) 250 [INSPIRE].

[37] S. Jadach, B.F.L. Ward and Z. Was, *The precision Monte Carlo event generator KK for two fermion final states in e^+e^- collisions*, *Comput. Phys. Commun.* **130** (2000) 260 [hep-ph/9912214] [INSPIRE].

[38] S. Jadach, B.F.L. Ward and Z. Was, *Coherent exclusive exponentiation for precision Monte Carlo calculations*, *Phys. Rev. D* **63** (2001) 113009 [hep-ph/0006359] [INSPIRE].

[39] G. D'Agostini, *On the use of the covariance matrix to fit correlated data*, *Nucl. Instrum. Meth. A* **346** (1994) 306 [INSPIRE].

[40] D.J. Lange, *The EvtGen particle decay simulation package*, *Nucl. Instrum. Meth. A* **462** (2001) 152 [INSPIRE].

[41] R.-G. Ping, *Event generators at BESIII*, *Chin. Phys. C* **32** (2008) 599 [INSPIRE].

[42] Particle Data Group collaboration, *Review of particle physics*, *PTEP* **2020** (2020) 083C01 [INSPIRE].

[43] J.C. Chen, G.S. Huang, X.R. Qi, D.H. Zhang and Y.S. Zhu, *Event generator for J/ψ and $\psi(2S)$ decay*, *Phys. Rev. D* **62** (2000) 034003 [INSPIRE].

[44] R.-L. Yang, R.-G. Ping and H. Chen, *Tuning and validation of the Lundcharm model with J/ψ decays*, *Chin. Phys. Lett.* **31** (2014) 061301 [INSPIRE].

[45] E. Richter-Was, *QED bremsstrahlung in semileptonic B and leptonic τ decays*, *Phys. Lett. B* **303** (1993) 163 [INSPIRE].

[46] ARGUS collaboration, *Search for hadronic $b \to u$ decays*, *Phys. Lett. B* **241** (1990) 278 [INSPIRE].

[47] Working Group on Radiative Corrections, Monte Carlo Generators for Low Energies collaboration, *Quest for precision in hadronic cross sections at low energy: Monte Carlo tools vs. experimental data*, *Eur. Phys. J. C* **66** (2010) 585 [arXiv:0912.0749] [INSPIRE].

[48] E.A. Kuraev and V.S. Fadin, *On radiative corrections to e^+e^- single photon annihilation at high-energy*, *Sov. J. Nucl. Phys.* **41** (1985) 466 [*Yad. Fiz.* **41** (1985) 733] [INSPIRE].

JHEP05(2022)155

[49] BESIII collaboration, *Search for hadronic transition $\chi_{cJ} \to \eta_c \pi^+ \pi^-$ and observation of $\chi_{cJ} \to K\overline{K}\pi\pi\pi$*, *Phys. Rev. D* **87** (2013) 012002 [arXiv:1208.4805] [INSPIRE].

[50] W.S. Cleveland, *Robust locally weighted regression and smoothing scatterplots*, *J. Amer. Statist. Assoc.* **74** (1979) 829.

[51] C.H. Reinsch, *Smoothing by spline functions*, *Numer. Math.* **10** (1967) 177.

[52] E. Eichten, K. Gottfried, T. Kinoshita, K.D. Lane and T.-M. Yan, *Charmonium: comparison with experiment*, *Phys. Rev. D* **21** (1980) 203 [INSPIRE].

JHEP05(2022)155

The BESIII collaboration

M. Ablikim[1], M. N. Achasov[10,b], P. Adlarson[68], M. Albrecht[4], R. Aliberti[28], A. Amoroso[67A,67C], M. R. An[32], Q. An[64,50], X. H. Bai[58], Y. Bai[49], O. Bakina[29], R. Baldini Ferroli[23A], I. Balossino[24A], Y. Ban[39,h], V. Batozskaya[1,37], D. Becker[28], K. Begzsuren[26], N. Berger[28], M. Bertani[23A], D. Bettoni[24A], F. Bianchi[67A,67C], J. Bloms[61], A. Bortone[67A,67C], I. Boyko[29], R. A. Briere[5], A. Brueggemann[61], H. Cai[69], X. Cai[1,50], A. Calcaterra[23A], G. F. Cao[1,55], N. Cao[1,55], S. A. Cetin[54A], J. F. Chang[1,50], W. L. Chang[1,55], G. Chelkov[29,a], C. Chen[36], G. Chen[1], H. S. Chen[1,55], M. L. Chen[1,50], S. J. Chen[35], T. Chen[1], X. R. Chen[25,55], X. T. Chen[1], Y. B. Chen[1,50], Z. J. Chen[20,i], W. S. Cheng[67C], X. Chu[36], G. Cibinetto[24A], F. Cossio[67C], J. J. Cui[42], H. L. Dai[1,50], J. P. Dai[71], A. Dbeyssi[14], R. E. de Boer[4], D. Dedovich[29], Z. Y. Deng[1], A. Denig[28], I. Denysenko[29], M. Destefanis[67A,67C], F. De Mori[67A,67C], Y. Ding[33], J. Dong[1,50], L. Y. Dong[1,55], M. Y. Dong[1,50,55], X. Dong[69], S. X. Du[73], P. Egorov[29,a], Y. L. Fan[69], J. Fang[1,50], S. S. Fang[1,55], W. X. Fang[1], Y. Fang[1], R. Farinelli[24A], L. Fava[67B,67C], F. Feldbauer[4], G. Felici[23A], C. Q. Feng[64,50], J. H. Feng[51], K Fischer[62], M. Fritsch[4], C. F. Fritzsch[61], C. D. Fu[1], H. Gao[55], Y. N. Gao[39,h], Yang Gao[64,50], S. Garbolino[67C], I. Garzia[24A,24B], P. T. Ge[69], C. Geng[51], E. M. Gersabeck[59], A Gilman[62], K. Goetzen[11], L. Gong[33], W. X. Gong[1,50], W. Gradl[28], M. Greco[67A,67C], M. H. Gu[1,50], C. Y Guan[1,55], A. Q. Guo[25,55], L. B. Guo[34], R. P. Guo[41], Y. P. Guo[9,g], A. Guskov[29,a], T. T. Han[42], W. Y. Han[32], X. Q. Hao[15], F. A. Harris[57], K. K. He[47], K. L. He[1,55], F. H. Heinsius[4], C. H. Heinz[28], Y. K. Heng[1,50,55], C. Herold[52], M. Himmelreich[11,e], T. Holtmann[4], G. Y. Hou[1,55], Y. R. Hou[55], Z. L. Hou[1], H. M. Hu[1,55], J. F. Hu[48,j], T. Hu[1,50,55], Y. Hu[1], G. S. Huang[64,50], K. X. Huang[51], L. Q. Huang[65], L. Q. Huang[25,55], X. T. Huang[42], Y. P. Huang[1], Z. Huang[39,h], T. Hussain[66], N Hüsken[22,28], W. Imoehl[22], M. Irshad[64,50], J. Jackson[22], S. Jaeger[4], S. Janchiv[26], Q. Ji[1], Q. P. Ji[15], X. B. Ji[1,55], X. L. Ji[1,50], Y. Y. Ji[42], Z. K. Jia[64,50], H. B. Jiang[42], S. S. Jiang[32], X. S. Jiang[1,50,55], Y. Jiang[55], J. B. Jiao[42], Z. Jiao[18], S. Jin[35], Y. Jin[58], M. Q. Jing[1,55], T. Johansson[68], N. Kalantar-Nayestanaki[56], X. S. Kang[33], R. Kappert[56], M. Kavatsyuk[56], B. C. Ke[73], I. K. Keshk[4], A. Khoukaz[61], P. Kiese[28], R. Kiuchi[1], R. Kliemt[11], L. Koch[30], O. B. Kolcu[54A], B. Kopf[4], M. Kuemmel[4], M. Kuessner[4], A. Kupsc[37,68], W. Kühn[30], J. J. Lane[59], J. S. Lange[30], P. Larin[14], A. Lavania[21], L. Lavezzi[67A,67C], Z. H. Lei[64,50], H. Leithoff[28], M. Lellmann[28], T. Lenz[28], C. Li[36], C. Li[40], C. H. Li[32], Cheng Li[64,50], D. M. Li[73], F. Li[1,50], G. Li[1], H. Li[44], H. Li[64,50], H. B. Li[1,55], H. J. Li[15], H. N. Li[48,j], J. Q. Li[4], J. S. Li[51], J. W. Li[42], Ke Li[1], L. J Li[1], L. K. Li[1], Lei Li[3], M. H. Li[36], P. R. Li[31,k,l], S. X. Li[9], S. Y. Li[53], T. Li[42], W. D. Li[1,55], W. G. Li[1], X. H. Li[64,50], X. L. Li[42], Xiaoyu Li[1,55], Z. Y. Li[51], H. Liang[1,55], H. Liang[64,50], H. Liang[27], Y. F. Liang[46], Y. T. Liang[25,55], G. R. Liao[12], L. Z. Liao[42], J. Libby[21], A. Limphirat[52], C. X. Lin[51], D. X. Lin[25,55], T. Lin[1], B. J. Liu[1], C. X. Liu[1], D. Liu[14,64], F. H. Liu[45], Fang Liu[1], Feng Liu[6], G. M. Liu[48,j], H. Liu[31,k,l], H. M. Liu[1,55], Huanhuan Liu[1], Huihui Liu[16], J. B. Liu[64,50], J. L. Liu[65], J. Y. Liu[1,55], K. Liu[1], K. Y. Liu[33], Ke Liu[17], L. Liu[64,50], M. H. Liu[9,g], P. L. Liu[1], Q. Liu[55], S. B. Liu[64,50], T. Liu[9,g], W. K. Liu[36], W. M. Liu[64,50], X. Liu[31,k,l], Y. Liu[31,k,l], Y. B. Liu[36], Z. A. Liu[1,50,55], Z. Q. Liu[42], X. C. Lou[1,50,55], F. X. Lu[51], H. J. Lu[18], J. G. Lu[1,50], X. L. Lu[1], Y. Lu[1], Y. P. Lu[1,50], Z. H. Lu[1], C. L. Luo[34], M. X. Luo[72], T. Luo[9,g], X. L. Luo[1,50], X. R. Lyu[55], Y. F. Lyu[36], F. C. Ma[33], H. L. Ma[1], L. L. Ma[42], M. M. Ma[1,55], Q. M. Ma[1], R. Q. Ma[1,55], R. T. Ma[55], X. Y. Ma[1,50], Y. Ma[39,h], F. E. Maas[14], M. Maggiora[67A,67C], S. Maldaner[4], S. Malde[62], Q. A. Malik[66], A. Mangoni[23B], Y. J. Mao[39,h], Z. P. Mao[1], S. Marcello[67A,67C], Z. X. Meng[58], J. G. Messchendorp[56,d], G. Mezzadri[24A], H. Miao[1], T. J. Min[35], R. E. Mitchell[22], X. H. Mo[1,50,55], N. Yu. Muchnoi[10,b], H. Muramatsu[60], Y. Nefedov[29], F. Nerling[11,e], I. B. Nikolaev[10,b], Z. Ning[1,50], S. Nisar[8,m], Y. Niu [42], S. L. Olsen[55], Q. Ouyang[1,50,55], S. Pacetti[23B,23C], X. Pan[9,g], Y. Pan[59], A. Pathak[1], A. Pathak[27], M. Pelizaeus[4], H. P. Peng[64,50], K. Peters[11,e], J. Pettersson[68],

JHEP05(2022)155

J. L. Ping[34], R. G. Ping[1,55], S. Plura[28], S. Pogodin[29], R. Poling[60], V. Prasad[64,50], F. Z. Qi[1], H. Qi[64,50], H. R. Qi[53], M. Qi[35], T. Y. Qi[9,g], S. Qian[1,50], W. B. Qian[55], Z. Qian[51], C. F. Qiao[55], J. J. Qin[65], L. Q. Qin[12], X. P. Qin[9,g], X. S. Qin[42], Z. H. Qin[1,50], J. F. Qiu[1], S. Q. Qu[53], S. Q. Qu[36], K. H. Rashid[66], C. F. Redmer[28], K. J. Ren[32], A. Rivetti[67C], V. Rodin[56], M. Rolo[67C], G. Rong[1,55], Ch. Rosner[14], S. N. Ruan[36], H. S. Sang[64], A. Sarantsev[29,c], Y. Schelhaas[28], C. Schnier[4], K. Schoenning[68], M. Scodeggio[24A,24B], K. Y. Shan[9,g], W. Shan[19], X. Y. Shan[64,50], J. F. Shangguan[47], L. G. Shao[1,55], M. Shao[64,50], C. P. Shen[9,g], H. F. Shen[1,55], X. Y. Shen[1,55], B.-A. Shi[55], H. C. Shi[64,50], J. Y. Shi[1], R. S. Shi[1,55], X. Shi[1,50], X. D Shi[64,50], J. J. Song[15], W. M. Song[27,1], Y. X. Song[39,h], S. Sosio[67A,67C], S. Spataro[67A,67C], F. Stieler[28], K. X. Su[69], P. P. Su[47], Y.-J. Su[55], G. X. Sun[1], H. Sun[55], H. K. Sun[1], J. F. Sun[15], L. Sun[69], S. S. Sun[1,55], T. Sun[1,55], W. Y. Sun[27], X Sun[20,i], Y. J. Sun[64,50], Y. Z. Sun[1], Z. T. Sun[42], Y. H. Tan[69], Y. X. Tan[64,50], C. J. Tang[46], G. Y. Tang[1], J. Tang[51], L. Y Tao[65], Q. T. Tao[20,i], J. X. Teng[64,50], V. Thoren[68], W. H. Tian[44], Y. Tian[25,55], I. Uman[54B], B. Wang[1], B. L. Wang[55], D. Y. Wang[39,h], F. Wang[65], H. J. Wang[31,k,l], H. P. Wang[1,55], K. Wang[1,50], L. L. Wang[1], M. Wang[42], M. Z. Wang[39,h], Meng Wang[1,55], S. Wang[9,g], T. Wang[9,g], T. J. Wang[36], W. Wang[51], W. H. Wang[69], W. P. Wang[64,50], X. Wang[39,h], X. F. Wang[31,k,l], X. L. Wang[9,g], Y. D. Wang[38], Y. F. Wang[1,50,55], Y. H. Wang[40], Y. Q. Wang[1], Ying Wang[51], Z. Wang[1,50], Z. Y. Wang[1,55], Ziyi Wang[55], D. H. Wei[12], F. Weidner[61], S. P. Wen[1], D. J. White[59], U. Wiedner[4], G. Wilkinson[62], M. Wolke[68], L. Wollenberg[4], J. F. Wu[1,55], L. H. Wu[1], L. J. Wu[1,55], X. Wu[9,g], X. H. Wu[27], Y. Wu[64], Z. Wu[1,50], L. Xia[64,50], T. Xiang[39,h], D. Xiao[31,k,l], H. Xiao[9,g], S. Y. Xiao[1], Y. L. Xiao[9,g], Z. J. Xiao[34], X. H. Xie[39,h], Y. Xie[42], Y. G. Xie[1,50], Y. H. Xie[6], Z. P. Xie[64,50], T. Y. Xing[1,55], C. F. Xu[1], C. J. Xu[51], G. F. Xu[1], Q. J. Xu[13], S. Y. Xu[63], X. P. Xu[47], Y. C. Xu[55], F. Yan[9,g], L. Yan[9,g], W. B. Yan[64,50], W. C. Yan[73], H. J. Yang[43,f], H. L. Yang[27], H. X. Yang[1], L. Yang[44], S. L. Yang[55], Tao Yang[1], Y. X. Yang[1,55], Yifan Yang[1,55], M. Ye[1,50], M. H. Ye[7], J. H. Yin[1], Z. Y. You[51], B. X. Yu[1,50,55], C. X. Yu[36], G. Yu[1,55], T. Yu[65], C. Z. Yuan[1,55], L. Yuan[2], S. C. Yuan[1], X. Q. Yuan[1], Y. Yuan[1,55], Z. Y. Yuan[51], C. X. Yue[32], A. A. Zafar[66], F. R. Zeng[42], X. Zeng Zeng[6], Y. Zeng[20,i], Y. H. Zhan[51], A. Q. Zhang[1], B. L. Zhang[1], B. X. Zhang[1], D. H. Zhang[36], G. Y. Zhang[15], H. Zhang[64], H. H. Zhang[51], H. H. Zhang[27], H. Y. Zhang[1,50], J. L. Zhang[70], J. Q. Zhang[34], J. W. Zhang[1,50,55], J. X. Zhang[31,k,l], J. Y. Zhang[1], J. Z. Zhang[1,55], Jianyu Zhang[1,55], Jiawei Zhang[1,55], L. M. Zhang[53], L. Q. Zhang[51], Lei Zhang[35], P. Zhang[1], Q. Y. Zhang[32,73], Shulei Zhang[20,i], X. D. Zhang[38], X. M. Zhang[1], X. Y. Zhang[42], X. Y. Zhang[47], Y. Zhang[62], Y. T. Zhang[73], Y. H. Zhang[1,50], Yan Zhang[64,50], Yao Zhang[1], Z. H. Zhang[1], Z. Y. Zhang[36], Z. Y. Zhang[69], G. Zhao[1], J. Zhao[32], J. Y. Zhao[1,55], J. Z. Zhao[1,50], Lei Zhao[64,50], Ling Zhao[1], M. G. Zhao[36], Q. Zhao[1], S. J. Zhao[73], Y. B. Zhao[1,50], Y. X. Zhao[25,55], Z. G. Zhao[64,50], A. Zhemchugov[29,a], B. Zheng[65], J. P. Zheng[1,50], Y. H. Zheng[55], B. Zhong[34], C. Zhong[65], X. Zhong[51], H. Zhou[42], L. P. Zhou[1,55], X. Zhou[69], X. K. Zhou[55], X. R. Zhou[64,50], X. Y. Zhou[32], Y. Z. Zhou[9,g], J. Zhu[36], K. Zhu[1], K. J. Zhu[1,50,55], L. X. Zhu[55], S. H. Zhu[63], T. J. Zhu[70], W. J. Zhu[9,g], Y. C. Zhu[64,50], Z. A. Zhu[1,55], B. S. Zou[1], J. H. Zou[1]

[1] *Institute of High Energy Physics, Beijing 100049, People's Republic of China*
[2] *Beihang University, Beijing 100191, People's Republic of China*
[3] *Beijing Institute of Petrochemical Technology, Beijing 102617, People's Republic of China*
[4] *Bochum Ruhr-University, D-44780 Bochum, Germany*
[5] *Carnegie Mellon University, Pittsburgh, Pennsylvania 15213, U.S.A.*
[6] *Central China Normal University, Wuhan 430079, People's Republic of China*
[7] *China Center of Advanced Science and Technology, Beijing 100190, People's Republic of China*
[8] *COMSATS University Islamabad, Lahore Campus, Defence Road, Off Raiwind Road, 54000 Lahore, Pakistan*
[9] *Fudan University, Shanghai 200433, People's Republic of China*

JHEP05(2022)155

[10] G.I. Budker Institute of Nuclear Physics SB RAS (BINP), Novosibirsk 630090, Russia
[11] GSI Helmholtzcentre for Heavy Ion Research GmbH, D-64291 Darmstadt, Germany
[12] Guangxi Normal University, Guilin 541004, People's Republic of China
[13] Hangzhou Normal University, Hangzhou 310036, People's Republic of China
[14] Helmholtz Institute Mainz, Staudinger Weg 18, D-55099 Mainz, Germany
[15] Henan Normal University, Xinxiang 453007, People's Republic of China
[16] Henan University of Science and Technology, Luoyang 471003, People's Republic of China
[17] Henan University of Technology, Zhengzhou 450001, People's Republic of China
[18] Huangshan College, Huangshan 245000, People's Republic of China
[19] Hunan Normal University, Changsha 410081, People's Republic of China
[20] Hunan University, Changsha 410082, People's Republic of China
[21] Indian Institute of Technology Madras, Chennai 600036, India
[22] Indiana University, Bloomington, Indiana 47405, U.S.A.
[23] INFN Laboratori Nazionali di Frascati , (A)INFN Laboratori Nazionali di Frascati, I-00044, Frascati, Italy; (B)INFN Sezione di Perugia, I-06100, Perugia, Italy; (C)University of Perugia, I-06100, Perugia, Italy
[24] INFN Sezione di Ferrara, (A)INFN Sezione di Ferrara, I-44122, Ferrara, Italy; (B)University of Ferrara, I-44122, Ferrara, Italy
[25] Institute of Modern Physics, Lanzhou 730000, People's Republic of China
[26] Institute of Physics and Technology, Peace Ave. 54B, Ulaanbaatar 13330, Mongolia
[27] Jilin University, Changchun 130012, People's Republic of China
[28] Johannes Gutenberg University of Mainz, Johann-Joachim-Becher-Weg 45, D-55099 Mainz, Germany
[29] Joint Institute for Nuclear Research, 141980 Dubna, Moscow region, Russia
[30] Justus-Liebig-Universitaet Giessen, II. Physikalisches Institut, Heinrich-Buff-Ring 16, D-35392 Giessen, Germany
[31] Lanzhou University, Lanzhou 730000, People's Republic of China
[32] Liaoning Normal University, Dalian 116029, People's Republic of China
[33] Liaoning University, Shenyang 110036, People's Republic of China
[34] Nanjing Normal University, Nanjing 210023, People's Republic of China
[35] Nanjing University, Nanjing 210093, People's Republic of China
[36] Nankai University, Tianjin 300071, People's Republic of China
[37] National Centre for Nuclear Research, Warsaw 02-093, Poland
[38] North China Electric Power University, Beijing 102206, People's Republic of China
[39] Peking University, Beijing 100871, People's Republic of China
[40] Qufu Normal University, Qufu 273165, People's Republic of China
[41] Shandong Normal University, Jinan 250014, People's Republic of China
[42] Shandong University, Jinan 250100, People's Republic of China
[43] Shanghai Jiao Tong University, Shanghai 200240, People's Republic of China
[44] Shanxi Normal University, Linfen 041004, People's Republic of China
[45] Shanxi University, Taiyuan 030006, People's Republic of China
[46] Sichuan University, Chengdu 610064, People's Republic of China
[47] Soochow University, Suzhou 215006, People's Republic of China
[48] South China Normal University, Guangzhou 510006, People's Republic of China
[49] Southeast University, Nanjing 211100, People's Republic of China
[50] State Key Laboratory of Particle Detection and Electronics, Beijing 100049, Hefei 230026, People's Republic of China
[51] Sun Yat-Sen University, Guangzhou 510275, People's Republic of China
[52] Suranaree University of Technology, University Avenue 111, Nakhon Ratchasima 30000, Thailand
[53] Tsinghua University, Beijing 100084, People's Republic of China
[54] Turkish Accelerator Center Particle Factory Group, (A)Istinye University, 34010, Istanbul, Turkey; (B)Near East University, Nicosia, North Cyprus, Mersin 10, Turkey

JHEP05(2022)155

[55] University of Chinese Academy of Sciences, Beijing 100049, People's Republic of China
[56] University of Groningen, NL-9747 AA Groningen, The Netherlands
[57] University of Hawaii, Honolulu, Hawaii 96822, U.S.A.
[58] University of Jinan, Jinan 250022, People's Republic of China
[59] University of Manchester, Oxford Road, Manchester, M13 9PL, United Kingdom
[60] University of Minnesota, Minneapolis, Minnesota 55455, U.S.A.
[61] University of Muenster, Wilhelm-Klemm-Str. 9, 48149 Muenster, Germany
[62] University of Oxford, Keble Rd, Oxford, OX13RH, U.K.
[63] University of Science and Technology Liaoning, Anshan 114051, People's Republic of China
[64] University of Science and Technology of China, Hefei 230026, People's Republic of China
[65] University of South China, Hengyang 421001, People's Republic of China
[66] University of the Punjab, Lahore-54590, Pakistan
[67] University of Turin and INFN, (A)University of Turin, I-10125, Turin, Italy; (B)University of Eastern Piedmont, I-15121, Alessandria, Italy; (C)INFN, I-10125, Turin, Italy
[68] Uppsala University, Box 516, SE-75120 Uppsala, Sweden
[69] Wuhan University, Wuhan 430072, People's Republic of China
[70] Xinyang Normal University, Xinyang 464000, People's Republic of China
[71] Yunnan University, Kunming 650500, People's Republic of China
[72] Zhejiang University, Hangzhou 310027, People's Republic of China
[73] Zhengzhou University, Zhengzhou 450001, People's Republic of China

[a] Also at the Moscow Institute of Physics and Technology, Moscow 141700, Russia
[b] Also at the Novosibirsk State University, Novosibirsk, 630090, Russia
[c] Also at the NRC "Kurchatov Institute", PNPI, 188300, Gatchina, Russia
[d] Currently at Istanbul Arel University, 34295 Istanbul, Turkey
[e] Also at Goethe University Frankfurt, 60323 Frankfurt am Main, Germany
[f] Also at Key Laboratory for Particle Physics, Astrophysics and Cosmology, Ministry of Education; Shanghai Key Laboratory for Particle Physics and Cosmology; Institute of Nuclear and Particle Physics, Shanghai 200240, People's Republic of China
[g] Also at Key Laboratory of Nuclear Physics and Ion-beam Application (MOE) and Institute of Modern Physics, Fudan University, Shanghai 200443, People's Republic of China
[h] Also at State Key Laboratory of Nuclear Physics and Technology, Peking University, Beijing 100871, People's Republic of China
[i] Also at School of Physics and Electronics, Hunan University, Changsha 410082, China
[j] Also at Guangdong Provincial Key Laboratory of Nuclear Science, Institute of Quantum Matter, South China Normal University, Guangzhou 510006, China
[k] Also at Frontiers Science Center for Rare Isotopes, Lanzhou University, Lanzhou 730000, People's Republic of China
[l] Also at Lanzhou Center for Theoretical Physics, Lanzhou University, Lanzhou 730000, People's Republic of China
[m] Also at the Department of Mathematical Sciences, IBA, Karachi , Pakistan

JHEP05(2022)155